Nordic nuclear safety research

NKS-308
ISBN 978-87-7893-386-7

CFD and FEM simulations of pressure suppression pool behaviour

Antti Timperi
Timo Pättikangas
Jarto Niemi

VTT Technical Research Centre of Finland

June 2014

Abstract

"The large interface model" published recently by P. Coste has been studied. The interface tracking model of Coste has been implemented in Fluent. The direct-contact condensation model has been modified so that the grid cells adjacent to the interface cell are also used in the heat transfer calculation. Simulations of short period of the chugging phase of the PPOOLEX experiment MIX-03 have been performed.

Modelling of the PPOOLEX experiment COL-01 has been performed with the acoustic-structural FEM model. Different values for the pool structural damping were first tested to find a damping value giving best agreement with the experiment. Simulations with three different values of water sonic speed have been performed and compared with the experiment. The effects of including the drywell gas to the acoustic model and applying the pressure source at the vent pipe outlet have been studied.

Studies of scaling of the measurements to full scale geometry have been performed. Simulations of the beginning of the blowdown have been performed with the new Star-CCM+ code and compared with the scaling results from 2012. Oscillation frequency of the water surface in the vent pipe has also been studied with an analytical model. The oscillation frequency has been calculated with Star-CCM+ and compared with the analytical results.

The coefficients for the Rayleigh damping of the structure have been studied. A mesh sensitivity study has been performed. Characterization of the pressure pulse has been started; simulations with different shapes of pressure pulses have been performed to study the effect of the shape. Convergence of the containment response statistics has been examined by evaluating the statistics for signals of different length.

Key words

Condensation pool, pressure suppression pool, BWR, CFD, fluid-structure interaction, FSI, chugging, LOCA

NKS-308
ISBN 978-87-7893-386-7

Electronic report, June 2014

NKS Secretariat
P.O. Box 49
DK - 4000 Roskilde, Denmark

Phone +45 4677 4041
www.nks.org
e-mail nks@nks.org

Acknowledgment

NKS conveys its gratitude to all organisations and persons who by means of financial support or contributions in kind have made the work presented in this report possible.

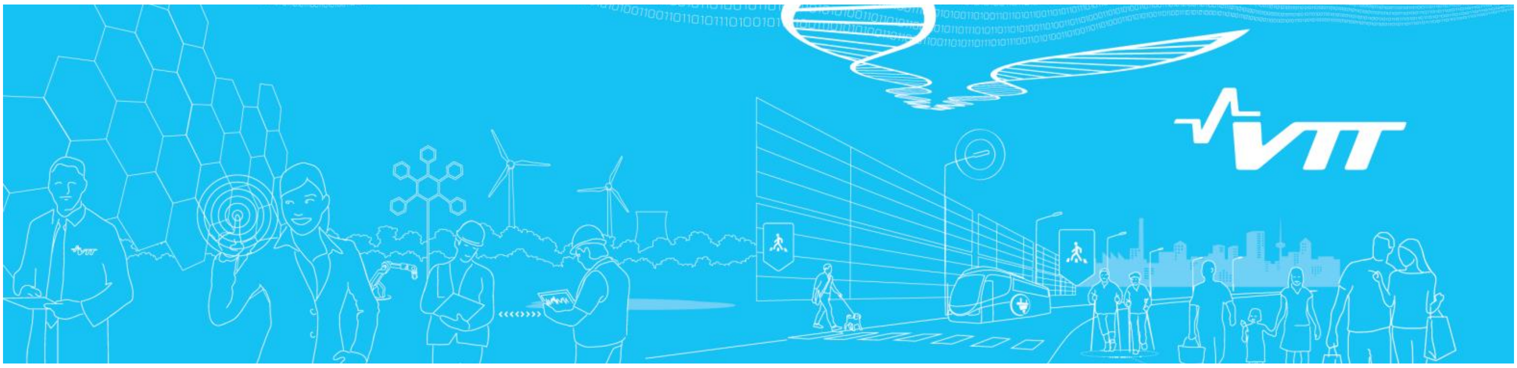

RESEARCH REPORT

VTT-R-00780-14

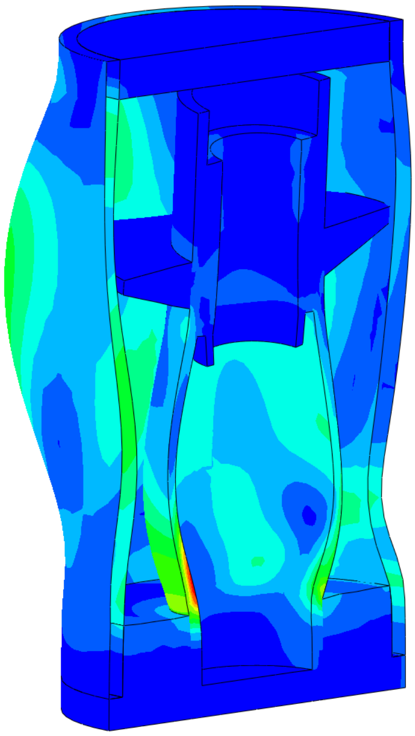

CFD and FEM simulations of pressure suppression pool behaviour

Authors: Antti Timperi, Timo Pättikangas and Jarto Niemi

Confidentiality: Public

Report's title	
CFD and FEM simulations of pressure suppression pool behaviour	
Customer, contact person, address	**Order reference**
1. Valtion ydinjätehuoltorahasto, Työ- ja elinkeinoministeriö, PL 32, 00023 VALTIONEUVOSTO 2. Karin Andgren, Nordic nuclear safety research (NKS), Programme Manager NKS-R, VATTENFALL, SE-169 92 Stockholm, SWEDEN	1. SAFIR2014 Programme: Dnro 24/2013SAF 2. NKS Contract no. AFT/NKS-R(13)90/7
Project name	**Project number/Short name**
Numerical modelling of condensation pool	77360 / NUMPOOL2013
Author(s)	**Pages**
Antti Timperi, Timo Pättikangas and Jarto Niemi	54/
Keywords	**Report identification code**
Condensation pool, pressure suppression pool, BWR, CFD, fluid-structure interaction, FSI, chugging, LOCA	VTT-R-00780-14

Summary

"The large interface model" published recently by P. Coste has been studied. The interface tracking model of Coste has been implemented in Fluent. The direct-contact condensation model has been modified so that the grid cells adjacent to the interface cell are also used in the heat transfer calculation. Simulations of short period of the chugging phase of the PPOOLEX experiment MIX-03 have been performed.

Modelling of the PPOOLEX experiment COL-01 has been performed with the acoustic-structural FEM model. Different values for the pool structural damping were first tested to find a damping value giving best agreement with the experiment. Simulations with three different values of water sonic speed have been performed and compared with the experiment. The effects of including the drywell gas to the acoustic model and applying the pressure source at the vent pipe outlet have been studied.

Studies of scaling of the measurements to full scale geometry have been performed. Simulations of the beginning of the blowdown have been performed with the new Star-CCM+ code and compared with the scaling results from 2012. Oscillation frequency of the water surface in the vent pipe has also been studied with an analytical model. The oscillation frequency has been calculated with Star-CCM+ and compared with the analytical results.

The coefficients for the Rayleigh damping of the structure have been studied. A mesh sensitivity study has been performed. Characterization of the pressure pulse has been started; simulations with different shapes of pressure pulses have been performed to study the effect of the shape. Convergence of the containment response statistics has been examined by evaluating the statistics for signals of different length.

Confidentiality	Public

Espoo, 20.4.2014

Written by	Reviewed by	Accepted by
Timo Pättikangas Principal Scientist	Mikko Manninen Principal Scientist	Jari Lehto Head of Research Area

VTT's contact address

VTT Technical Research Centre of Finland, P.O.B. 1000, FI-02044 VTT, Finland

Distribution (customer and VTT)

Karin Andgren (NKS), STUK, Vesa Suolanen (VTT), Pavel Kudinov (KTH), Vesa Tanskanen (LUT), Markku Puustinen (LUT), Heikki Purhonen (LUT), Jani Laine (LUT), SAFIR2014 Reference Group 4

Preface

This work has been carried out in the NUMPOOL project of the SAFIR2014 programme (The Finnish Research Programme on Nuclear Power Plant Safety). The project has been funded by Valtion ydinjätehuoltorahasto, VTT and NKS (Nordic nuclear safety research). The authors are grateful for comments obtained from the members of the SAFIR2010 Reference Group 4 and from the Northnet Roadmap 3 Reference Group.

Espoo 28.3.2014

Authors

Contents

1. Introduction

In boiling water reactors (BWRs), the major function of the containment system is to protect the environment if a loss-of-coolant accident (LOCA) should occur. The containment is designed to accommodate the loads generated in hypothetical accidents, such as sudden rupture of a main steam line. In such an accident, a large amount of steam is suddenly released in the containment. An essential part of the pressure suppression containment is a water pool, where condensation of released steam occurs.

In a BWR, the pressure suppression containment typically consists of a drywell and a wetwell with a water pool. In the hypothetical LOCA, steam and air flow from the drywell through vent pipes to the wetwell, where the outlets of the vent pipes are submerged in the water pool. In the early part of the accident, mainly non-condensable air or nitrogen flows through the vent pipes into the wetwell. Then, the volume fraction of vapor increases in the gas mixture. When all the non-condensable gas from the drywell has been blown into the wetwell, the blowdown consists of pure vapor. At this stage, so-called chugging effect may occur, which means periodic formation and rapid condensation of large vapor bubbles at the vent outlets (Lahey and Moody, 1993). The rapid condensation of the vapor bubbles may induce significant pressure loads on the structures in the pressure suppression pool and on the containment.

Determination of the chugging pressure source from the PPOOLEX experiments is studied with the acoustic-structural FSI model. The time signal for the pressure source is taken from pressure signal measured near the vent pipe exit for a rapidly collapsing steam bubble. The linearity of the FSI model enables linear scaling of the load magnitude and the pool response. Hence the pressure source magnitude is scaled according to measured pool pressures and displacements. Different water sonic velocities and ways for applying the pressure source at the vent exit as well as the effect of the containment gas volumes are studied in the modelling.

The scaling of the measured pressure loads to full-scale was studied in the previous work by review of the Sonin (1981) dimensional analysis and by dimensional analyses of various phenomena during the air and steam discharge (Timperi et al., 2013). In this work, these scaling results are tested by CFD and analytical calculations. The considered cases are the initial non-condensable phase of air discharge through the vent pipes as well as oscillation of the water surface in the vent pipe and of the bubble.

Stochastic simulations of the BWR containment are continued by using the acoustic FSI model developed in the previous work (Timperi et al., 2013). The model and the simulations are first verified and improved. Mesh sensitivity for the pool water is studied, since a fairly coarse mesh is used in the simplified model. Statistics of the pool structural response are evaluated for different simulation durations in order to have a reasonable duration. The pool structural damping is adjusted according to the most important pool eigenfrequencies. Characterization of the load shape of the chug events and simulations with different load shapes are then performed. In the previous work, the load shape was scaled to full-scale from the PPOOLEX experiments. In this work, the load shape is determined from the full-scale JAERI experiments presented by Kukita and Namatame (1985), which show somewhat different load shapes compared to the PPOOLEX experiments. The stochastic simulations are performed with different load shapes using two different water sonic velocities and the results are compared.

2. FSI calculations of chugging pressure source

The PPOOLEX experiment COL-01 was analysed in earlier work by Timperi et al. (2012). Bubble collapses giving the largest pressure loads were searched from the measurements and analysed. In the following, the acoustic-structural FSI model is used for determining the pressure source magnitude from the experiment.

2.1 FEM models

The acoustic-structural FEM model of the PPOOLEX facility is shown in Fig. 1. The structural model consists of about 15000 shell elements and of about 100 beam elements, whereas the water mesh consists of about 38000 hexahedral acoustic elements. The separate acoustic FEM model including also gas volumes of the facility is shown in Fig. 2; the model consists of about 136000 hexahedral acoustic elements. In the acoustic model including the gas volumes, the whole vent pipe is assumed to consist of gas since chugging is considered. In the following, the models are denoted as follows:

- Model 1: acoustic-structural FSI model (Fig. 1).
- Model 2: acoustic model of the pool water (Fig. 1).
- Model 3: acoustic model of the pool including also gas volumes (Fig. 2).

Flexibility of the disc springs and base structures under the four vertical support columns were modelled with linear springs. Values k = 21 MN/m and γ = 12 kNs/m were used for the spring stiffness and damping coefficient, respectively. The value for the spring stiffness has been chosen so that the frequency of the vertical oscillation of the whole pool corresponds to the experimentally observed value, i.e. about 11 Hz. In addition, the damping value of the springs has been chosen so that the damping of the vertical oscillation is similar to the experiments.

In the structure, values ρ = 7850 kg/m^3, E = 206 GPa and ν = 0.3 were used for density, Young's modulus and Poisson's ratio, respectively. Damping in the structure material was applied in order to have similar pool wall damping in the calculations as observed in the measurements. The Rayleigh damping parameter was set to $\beta = 5\times10^{-5}$, as described in the next section.

For water, value ρ = 1000 kg/m^3 was used for density, while values K = 2.224, 1.0 or 0.49 GPa were used for bulk modulus corresponding to speeds of sound $c_w = \sqrt{K/\rho}$ = 1491, 1000 or 700 m/s, respectively. In the experiment COL-01 during the chugging phase, steam pressure and temperature measured in the vent pipe were about p = 2.8 bar and T = 132 °C, respectively (Laine et al., 2009). According to the ideal gas law, the steam density is then set to ρ = 1.5 kg/m^3. The speed of sound in ideal gas is $c_g = \sqrt{\gamma p/\rho}$, γ being the specific heat ratio (Wiksten, 1995). Applying for steam γ = 1.3, we have c_g = 493 m/s and K = 0.364 MPa.

The volume acceleration was set as loading at the exit of the vent pipe. The time signal for the volume acceleration was taken by linearly scaling the pressure measured at sensor P5 for the bubble collapse. The normalized volume acceleration is shown in Fig. 3. Due to linearity of the acoustic-structural model, the results are linearly dependent on the magnitude of the load. Three different locations for the load were considered as shown in Fig. 4. In Load 1, the load is applied to all nodes at the vent pipe exit, while in the other cases rings of nodes at the pipe outer surface are considered. The latter cases were included to reflect the fact that the collapsing bubbles had a toroidal shape (Laine et al., 2009; Timperi et al., 2012). The total volume acceleration is sum of the nodal load values, so that the volume acceleration applied per node varies between the cases with different node numbers. Load 2 and Load 3 were used only in Model 3.

The analyses were carried out by using implicit direct time integration. Time step in the simulations was 0.02 ms. Pressure sensor locations in the FEM models are shown in Fig. 5.

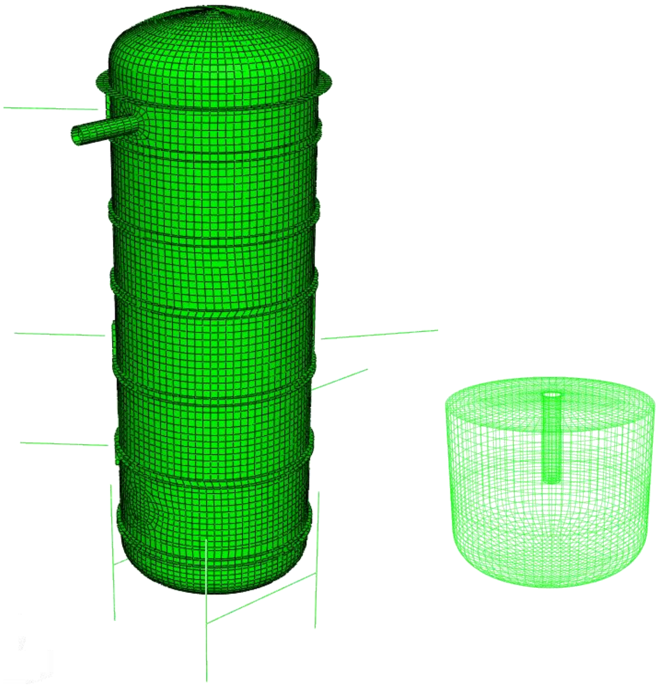

Figure 1. Structural (left) and acoustic water (right) models of the PPOOLEX facility.

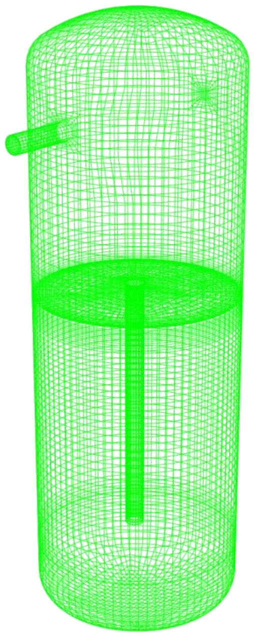

Figure 2. Acoustic model of the PPOOLEX facility including wetwell and drywell.

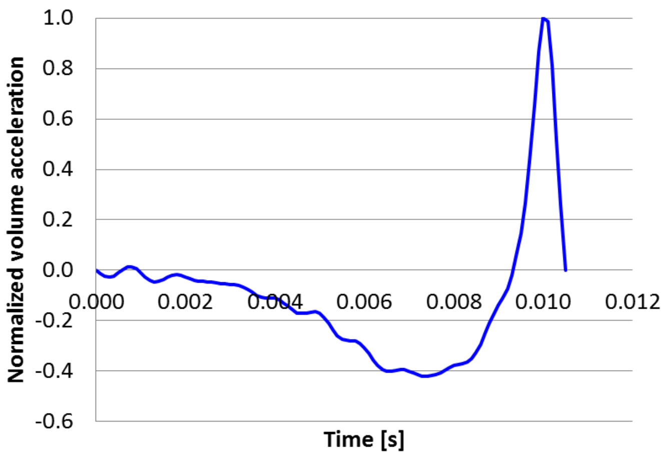

Figure 3. Normalized volume acceleration used as loading in the PPOOLEX model.

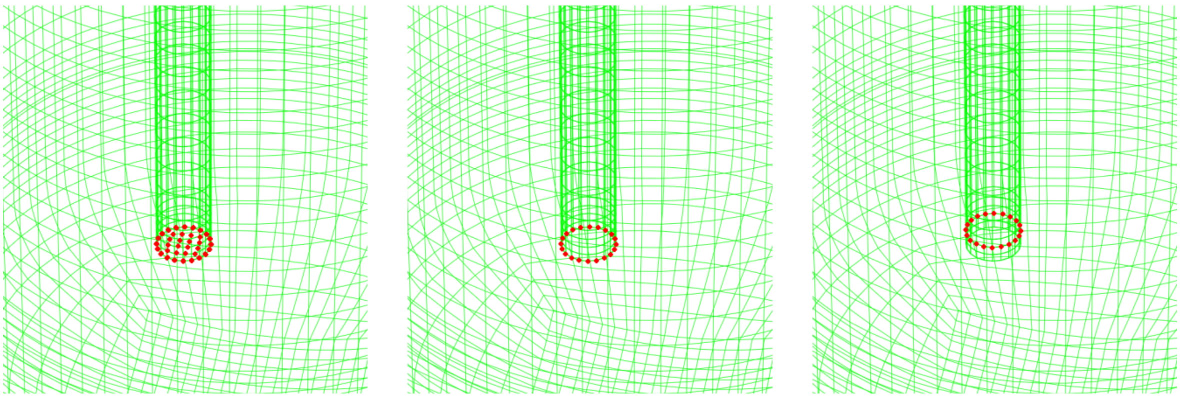

Figure 4. Node sets for volume acceleration loading. From left: Load 1, Load 2 and Load 3.

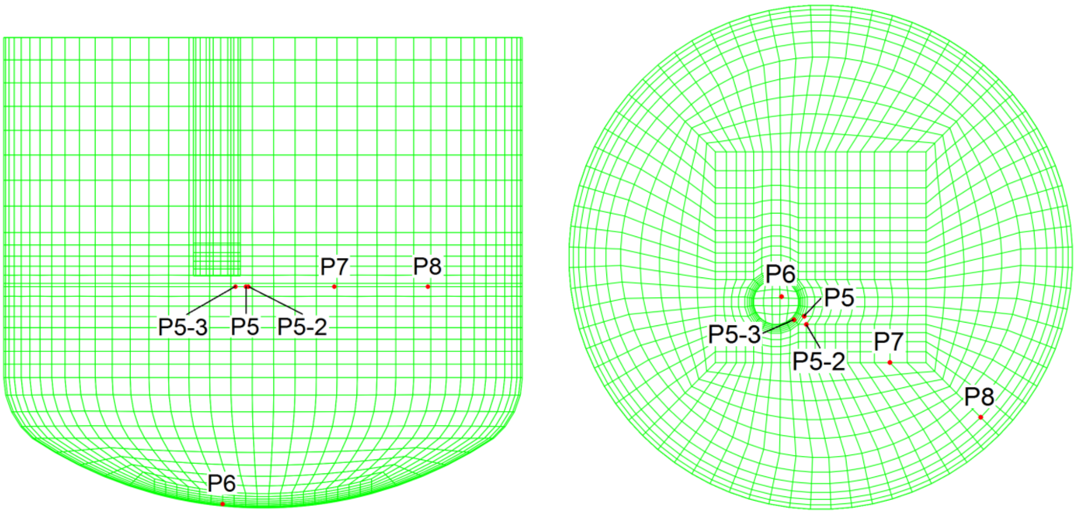

Figure 5. Locations of pressure sensors in the FEM models.

2.2 Pool structural damping

Damping in the pool structures was adjusted to have approximately similar damping rate for the pool bottom flexural motion as is observed in the measurements. The Rayleigh damping was applied, which consists of specifying two damping parameters for the structure material: α for mass proportional damping and β for stiffness proportional damping. The damping matrix becomes

$$\mathbf{C} = \alpha\mathbf{M} + \beta\mathbf{K} \tag{1}$$

where **M** is the mass matrix and **K** is the stiffness matrix. With the Rayleigh damping, the equation of motion for the structure is

$$\mathbf{M}\ddot{u} + (\alpha\mathbf{M} + \beta\mathbf{K})\dot{u} + \mathbf{K}u = F(t) \tag{2}$$

where u is the displacement vector, F is the load vector, t is time and the dots denote differentiation with respect to time. For oscillation mode at angular frequency ω_i, the fraction of critical damping becomes

$$\zeta_i = \frac{\alpha}{2\omega_i} + \frac{\beta\omega_i}{2} \tag{3}$$

Thus, α is responsible for the effective damping of low-frequency motions, while β of high-frequency motions. In this work, we apply for simplicity only high-frequency damping, i.e. α is set to zero and β is specified.

Fig. 6 shows displacement at the pool bottom centre for four different steam bubble collapses in the COL-01 experiment, as well as corresponding FEM results with Model 1 using four different values for β. The load signal has been taken from the first measured bubble collapse. In the plots, the low-frequency motion at about 11 Hz is caused by flexing of the horizontal support structures and disc springs under the vertical support columns (vertical motion of the whole pool), while the high-frequency oscillation at about 150 Hz is flexure of the pool bottom wall. In reference to the load signal, the positive displacement at the early phase is presumably caused by the low-pressure phase of the bubble collapse. Based on the results, the stiffness of the pool bottom wall appears to be lower in the experiment compared to the FEM model. The largest value of β is clearly too high, while with $\beta = 5\times10^{-5}$, the flexural motion of the pool bottom wall damps out overall at a similar rate as in the experiment.

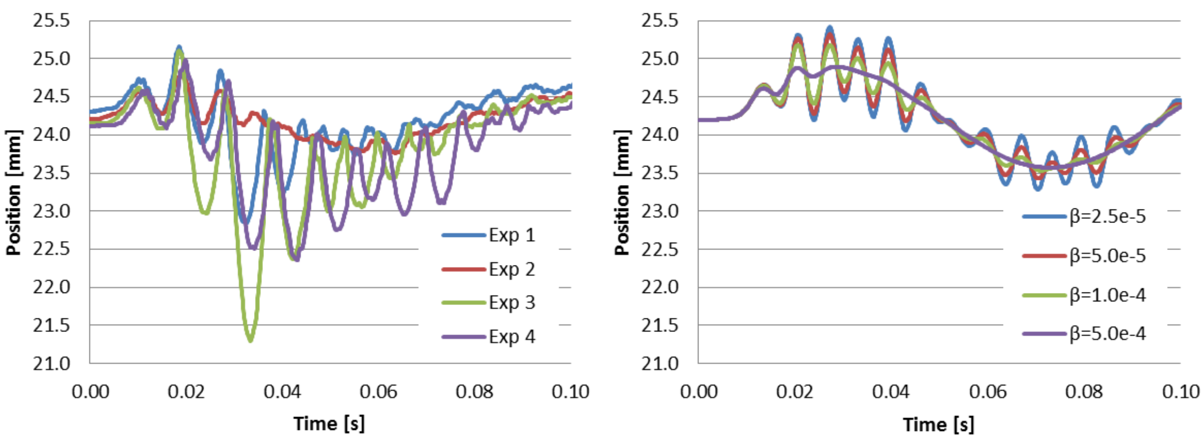

Figure 6. Comparison of pool bottom centre vertical displacement in PPOOLEX experiment COL-01 (left) and in FEM simulation with different values of structural damping (right).

2.3 Results

In the following, the volume acceleration for each case has been scaled so that the calculated peak pressure at P5 matches the experiment. The P5 sensor lies close to the vent pipe exit and hence the pressure amplitude is sensitive to the exact location of the sensor.

This is shown in Fig. 7, where the calculated pressures at P5, P5-2 and P5-3 are compared for Model 1 with water sonic velocity c_w = 1491 m/s. As shown below, a better way of scaling the load might be to use the sensors away from the vent pipe exit, e.g. sensor P8.

Figs. 8 and 9 compare calculated and measured pressures, displacements and accelerations for Model 1 with c_w = 1491 m/s and 700 m/s. For P5, the calculations match the experiment for the first under-pressure and first peak pressure, but the subsequent measured oscillations are not shown in the calculations. For P6, P7 and P8, magnitude of the under-pressure is predicted correctly while the peak pressure is too low. Timing of the pressure fluctuations appears to be better with c_w = 1491 m/s for P6 and P7, but better with c_w = 700 m/s for P8. For the pool bottom centre displacement, magnitude of the high-frequency oscillations is under-predicted, which may be due to too high stiffness of the pool wall in the FEM model. The magnitude of the pool bottom centre acceleration is fairly correct in the calculations. If the load scaling were done by matching the peak pressure e.g. at P8 instead of P5, we would obtain about 75 % higher scaling factor, but then magnitudes of the under-pressures in all sensors would be too high.

The effect of FSI is shown in Fig. 10, where the pressures for Model 1 and Model 2 are compared for c_w = 1491 m/s. For P5, the case without FSI shows oscillations after the peak pressure, but frequency of the oscillations is too low compared to the experiment. The effect of FSI is fairly large and the pressures are expectedly higher without FSI, where rigid walls are assumed. Timing of the pressure fluctuations is worse without FSI, especially for P6.

Fig. 11 compares the acoustic models without FSI, i.e. Model 2 with Load 1 and Model 3 with Load 1, Load 2 and Load 3. All cases are with c_w = 1491 m/s. By comparing the calculations with Load 1, it is seen that effect of including the gas volumes in the model is fairly significant, in particular for P5. Also, by comparing the models with gas volumes using the different loads, it is seen that the results are dependent on how the load is applied at the vent pipe exit.

Table 1 shows volume accelerations for the different cases when the first peak pressure at P5 or P8 has been matched with the experiment. As already noted above, different values for the volume acceleration are obtained by using different sensor for matching the results. The volume accelerations between different models vary significantly, especially when comparing the cases with and without the gas volumes. Here the gas volume has a significant effect since when it is included, part of the volume acceleration is involved in creating acoustic pressure in the gas inside the vent pipe. Without the gas volumes, the acoustic model boundary is at the vent pipe exit and hence all of the volume acceleration is involved in creating acoustic pressure in the pool water, thus requiring smaller volume acceleration for a given pressure amplitude in the pool water. The results show that magnitude of the volume acceleration to be used in a simulation depends on the modelling details, i.e. whether the gas volumes are included and how the load is applied at the vent pipe exit.

For a point pressure source in infinite fluid, the pressure amplitude is (Pättikangas et al., 2011)

$$\hat{p} = \frac{\rho \hat{\ddot{V}}}{4\pi r} \tag{4}$$

where ρ is the water density, r is the radial distance and $\hat{\ddot{V}}$ is the volume acceleration amplitude. The pressure sensors P6 and P8 are roughly 1 m away from the vent pipe exit. By applying the volume acceleration values 218 - 8506 m^3/s^2, Eq. (4) yields about 0.17 - 6.8 bar. However, Eq. (4) is not well applicable here due to the vent pipe and the finite extent of the pool.

Table 1. Volume accelerations obtained from different calculations when the first peak pressure at P5 or P8 has been matched with the experiment.

Model	FSI	Gas volumes	c_w [m/s]	Load	Volume acceleration [m^3/s^2]	
					P5	P8
1	Yes	No	700	1	406	643
	Yes	No	1000	1	389	652
	Yes	No	1491	1	390	679
2	No	No	1491	1	353	218
3	No	Yes	1491	1	8506	4114
	No	Yes	1491	2	2300	1289
	No	Yes	1491	3	1125	374

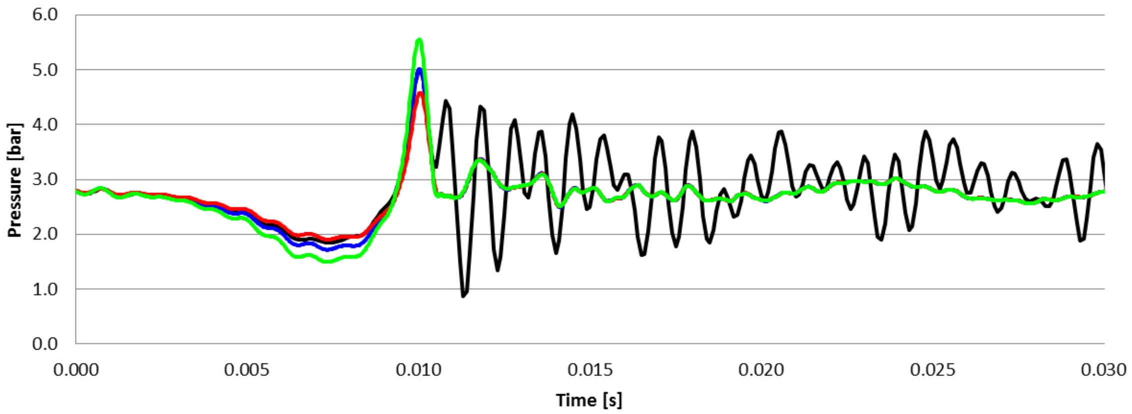

Figure 7. Calculated (c_w = 1491 m/s) and measured pressures at sensors P5, P5-2 and P5-3. (— Model 1 P5, — Model 1 P5-2, — Model 1 P5-3, — Experiment P5)

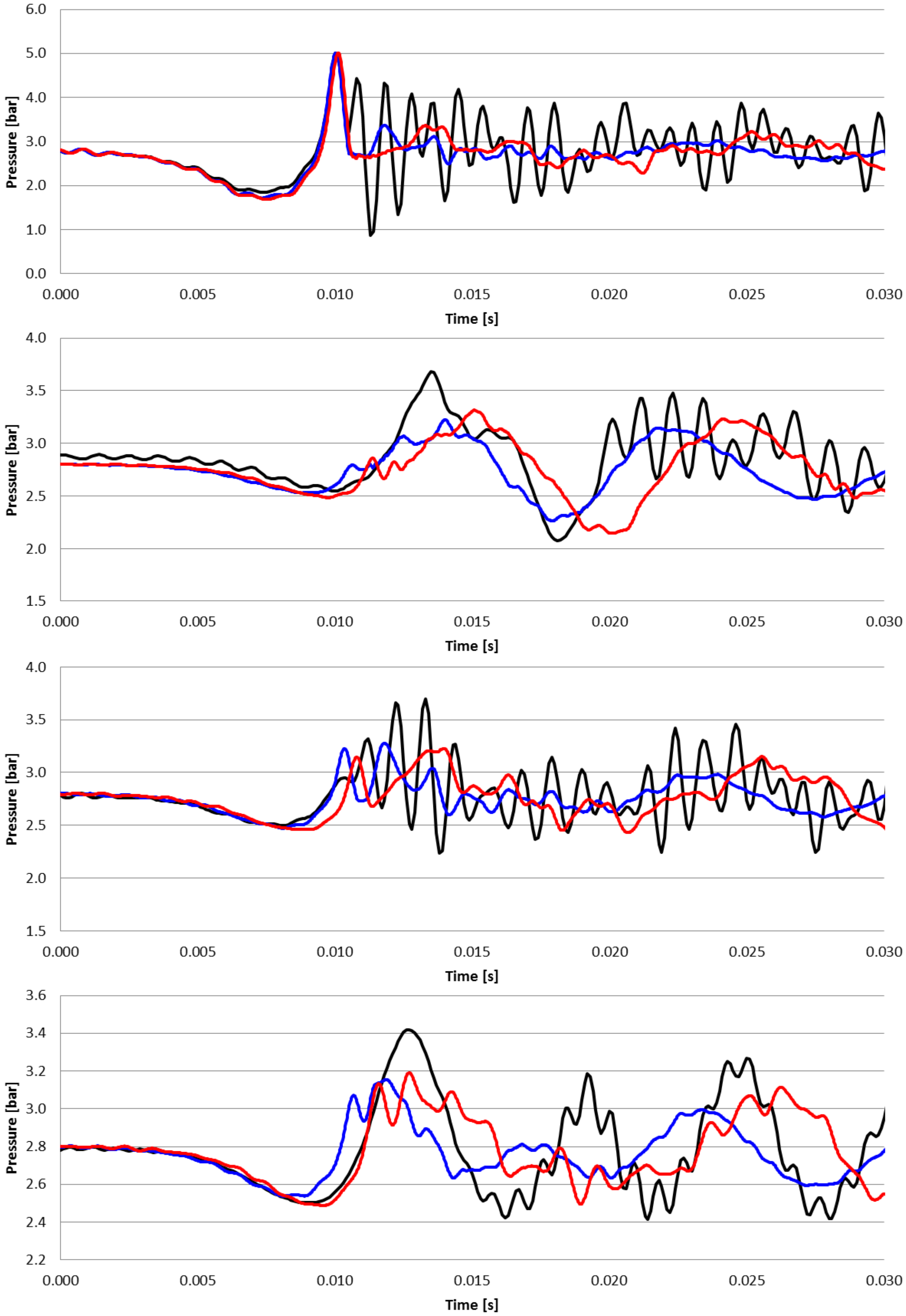

Figure 8. Calculated and measured pressures. From top: P5, P6, P7 and P8. (— Model 1 c_w = 1491 m/s, — Model 1 c_w = 700 m/s, — Experiment)

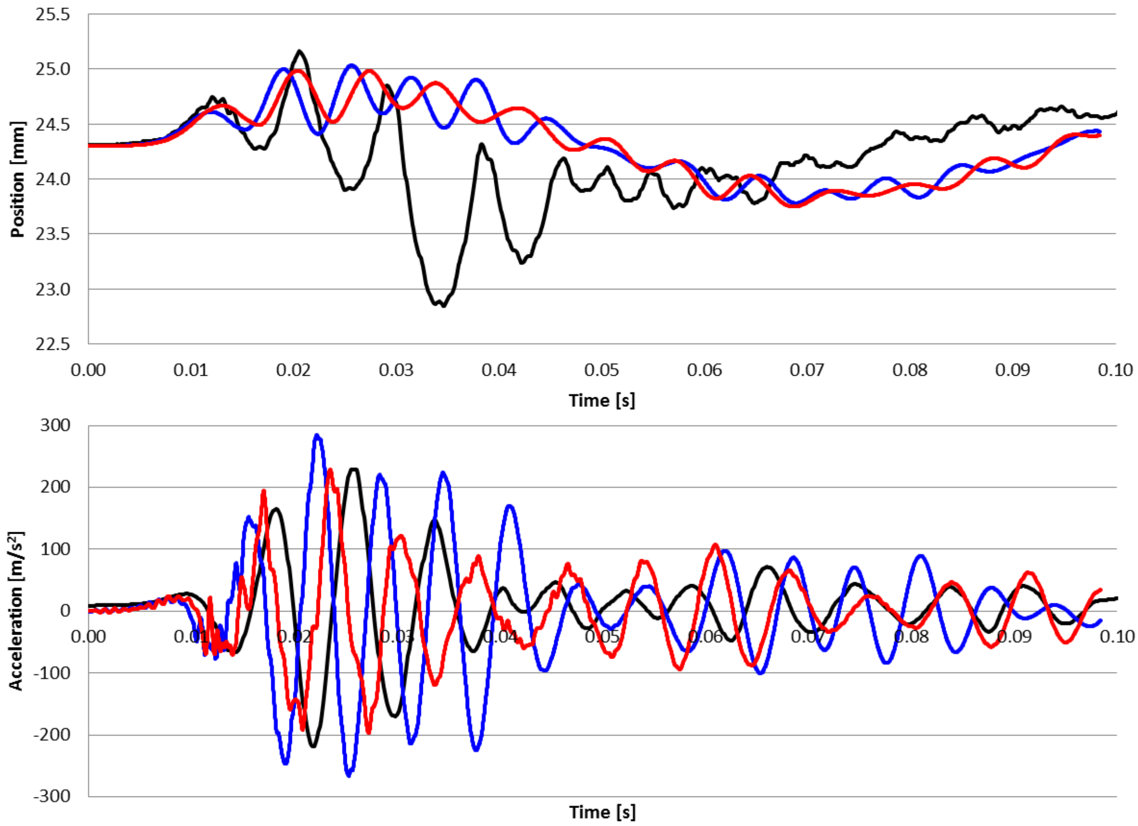

Figure 9. Pool bottom centre displacement (top) and acceleration (bottom). (— Model 1 c_w = 1491 m/s, — Model 1 c_w = 700 m/s, — Experiment)

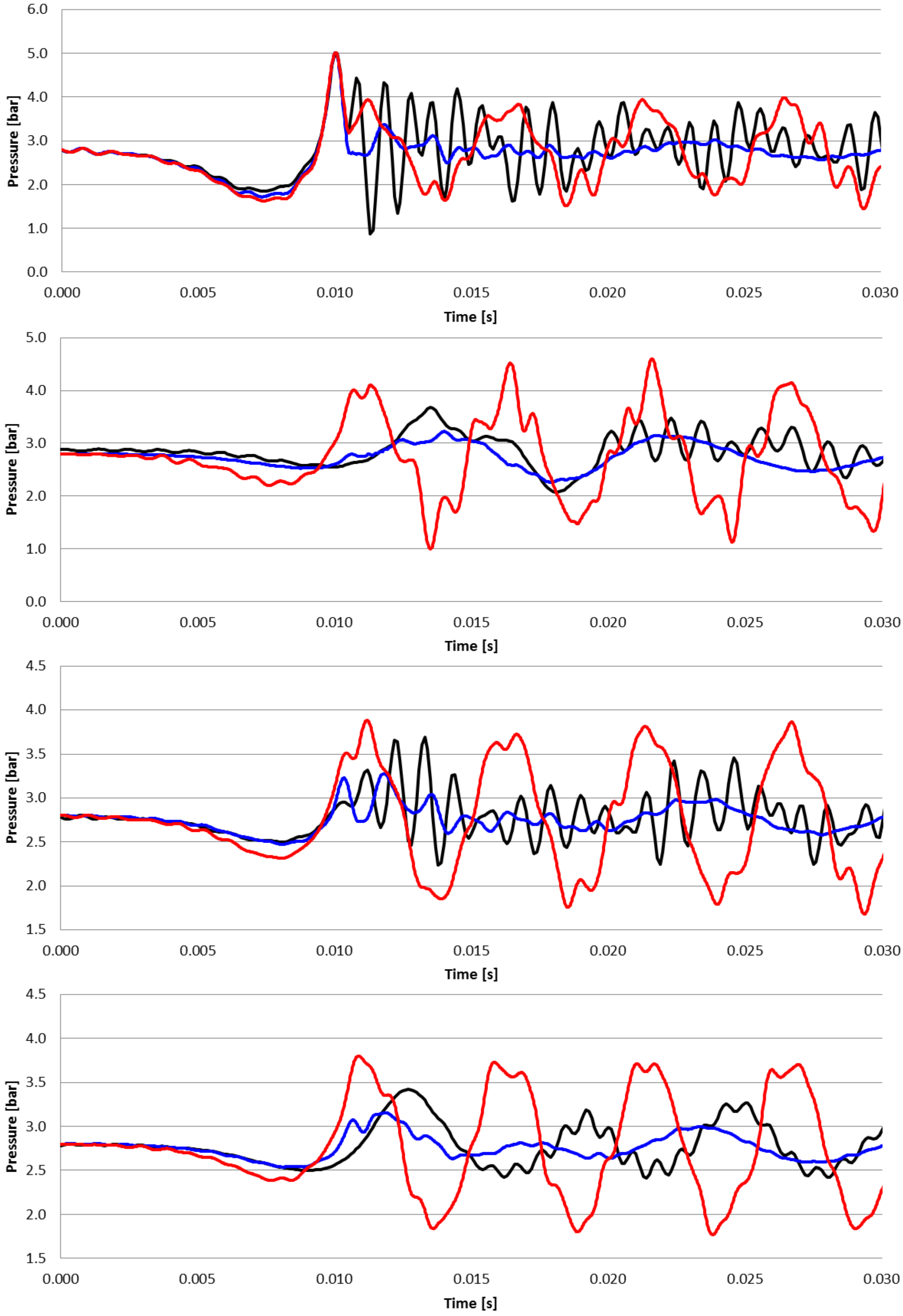

Figure 10. Calculated (c_w = 1491 m/s) and measured pressures. From top: P5, P6, P7 and P8. (— Model 1, — Model 2, — Experiment)

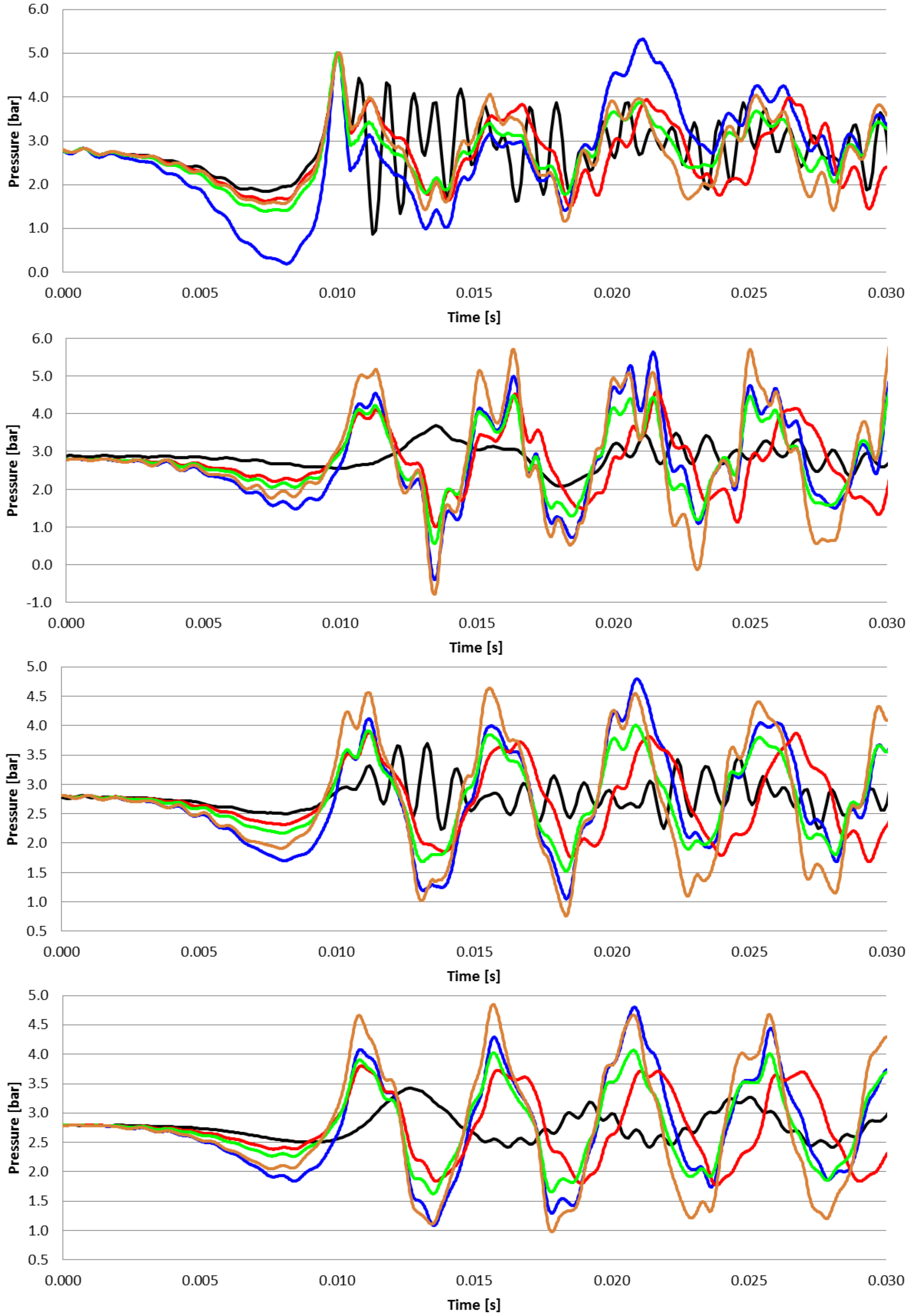

Figure 11. Calculated (c_w = 1491 m/s) and measured pressures. From top: P5, P6, P7 and P8. (— Model 2 Load 1, — Model 3 Load 1, — Model 3 Load 2, — Model 3 Load 3, — Experiment)

3. Scaling studies

Dimensional analysis of the discharge of steam into the condensation pool through a safety relief valve (SRV) was performed by Sonin (1981), while dimensional analysis of the vent clearing transient by air was performed by Timperi et al. (2013). The main assumptions used in the analyses were:

- The small- and full-scale facilities are geometrically identical.
- Same fluids are used in both systems.
- Both systems operate at the same thermodynamic conditions, i.e. pressures and temperatures.
- Gravitational effects can be neglected.

The assumption of negligible gravitation may not be valid for the initial discharge or steam chugging in the case of the open vent pipes, as discussed in Timperi et al. (2013) and in Sec. 3.1.2. For other important assumptions, see Sonin (1981) and Timperi et al. (2013). The both analyses showed the following scaling properties:

- Pressures, temperatures and velocities measured from the small-scale have same magnitudes as in full-scale at corresponding locations.
- Time, e.g. pressure pulse duration and frequencies, scales in linear proportion to the system size.

In addition, the dimensional analysis of the rise of large bubbles in the pool by Timperi et al. (2013), where gravity is an essential parameter, showed that both the bubble rise velocity u and time t scale in proportion to the square-root of the bubble size. Assuming that the bubble size is directly related to the system size L, we have for the bubble rise $u \sim \sqrt{L}$ and $t \sim \sqrt{L}$. Thus, rise of the large bubbles are miss-scaled in the above discharge analyses, where it is assumed that $t \sim L$. With the linear time dependency, the bubble would rise too slowly in the small-scale compared to full-scale, as noted also by Sonin (1981).

The natural oscillation frequency of the water surface in the vent pipe is studied analytically in Appendix A, showing different scaling results depending on the parameters. When the gravitational effect is significant, we have for the oscillation $t \sim \sqrt{L}$. On the other hand, when the pressure effect is significant, time of the oscillation scales linearly as $t \sim L$.

In the following, we study the scaling results for the initial air discharge phase and for the oscillation by performing CFD calculations with the Star-CCM+ 8.06 code.

3.1 Discharge transient

3.1.1 CFD model

The axisymmetric model of the PPOOLEX facility is shown in Fig. 12. The dimensions are same as in the real facility, but the pool bottom has been approximated by a straight wall. The volume of water is approximately same as for the real facility. Due to the axisymmetry, the vent pipe has been modelled at the symmetry axis contrary to the real facility. The wetwell is open since incompressible air is modelled. Cell size near the vent pipe outlet is 10 mm, while the maximum size in the wetwell water is 90 mm.

The Volume Of Fluid (VOF) model was used for tracking the free surface and the standard k-ε model and wall functions were used for modelling turbulence. Both air and water were assumed incompressible. A constant air velocity of 20 m/s was set at the vent pipe inlet. Time step was varied between 0.025 - 0.2 ms.

Incompressible air and a velocity boundary condition are required instead of compressible air and pressure boundary condition. This is because here the effect of hydrostatic pressure caused by the pipe submergence depth is comparable to the drywell pressurization, and hence the assumption of negligible gravitation in the dimensional analysis cannot be justified even for the initial discharge phase, as discussed in the next section. This was also confirmed in test calculations, where the drywell was included in the model and compressible air and pressure boundary condition were used.

To obtain the large-scale pool from the small-scale one, we use a scaling factor of 3, since the model of the PPOOLEX facility has a vent pipe diameter of about 200 mm, while e.g. the Olkiluoto 1 and 2 BWR pools have a vent pipe diameter of about 600 mm. Note, however, that somewhat different scaling factors could be obtained by using another parameter than the vent pipe diameter. The whole CFD model, time step and simulation time are scaled up with the scaling factor. The inlet velocity is set same in both small-scale and large-scale according to the dimensional analysis.

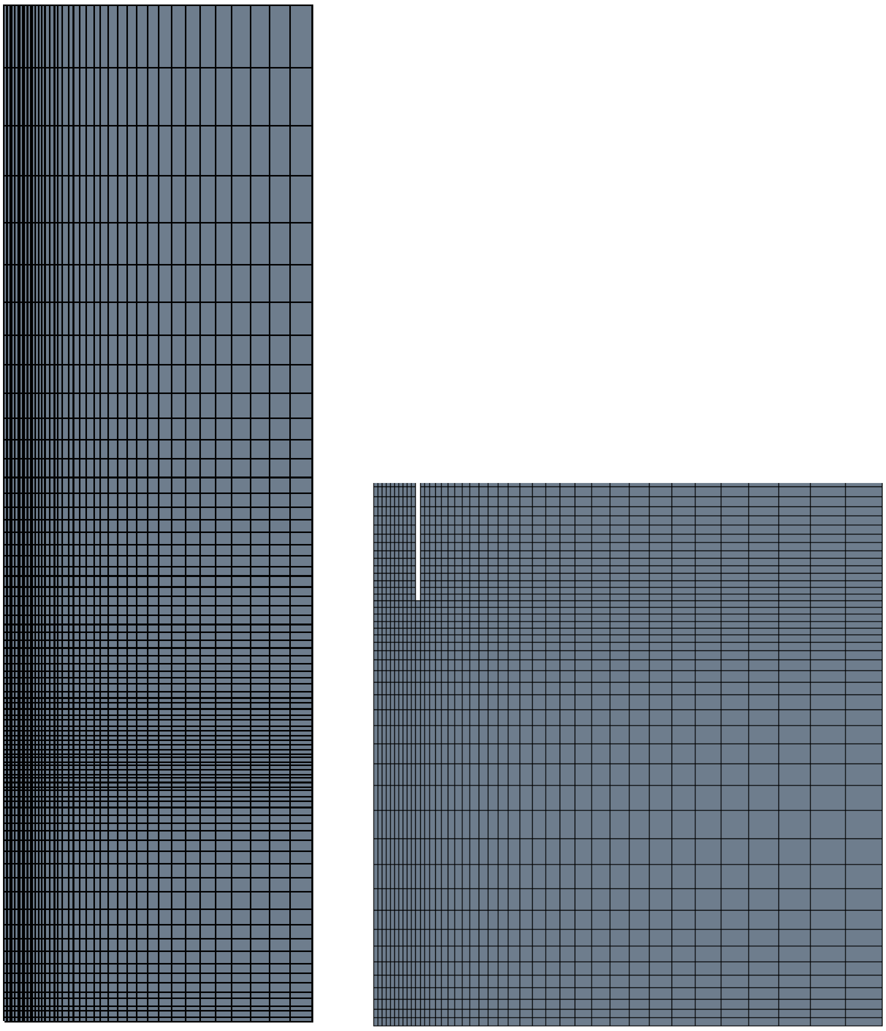

Figure 12. Axisymmetric CFD model without drywell for the PPOOLEX facility. On the left: overall mesh, on the right: detail of the mesh at pool water.

3.1.2 Results

Fig. 13 compares the first bubble for the small and large scale at corresponding times using the linear scaling $t \sim L$. Initially both cases are fairly similar, since the gravitational effect is small in the early phase of the transient. However, the subsequent bubble rise causes differences since the bubble rise is too slow in the small scale as predicted by the dimensional analysis, i.e. $t \sim \sqrt{L}$ for bubble rise.

The pool bottom average pressures are compared in Fig. 14, where time of the large scale has been transformed to the small scale using $t \sim L$. The pressure axis is unmodified as required by the dimensional analysis, except that the pressure levels have been aligned by taking into account the different hydrostatic pressure. The first pressure rise due to the vent clearing scales properly, but there are some differences in the subsequent low-pressure peak. The low-pressure peak seems to be artificially large and sharp, probably caused by the assumption of incompressible air. Namely in corresponding simulations with compressible air, the low-pressure peak has been wider and of similar magnitude as the over-pressure peak (see e.g. Timperi, 2009). The low-pressure peak is also sensitive to the analysis settings as shown in Fig. 15, where different time steps and iterations inside time are compared for the small scale. Generally larger pressure amplitudes are obtained when the number of iterations is increased or when the time step is decreased. When considering times t = 0…2 s in Fig. 14, the higher frequency due to the more rapid bubble shedding in the large scale can be seen, showing again that the linear scaling $t \sim L$ does not work when gravitational effects are significant.

For discharge through the open vent pipes, gravitational pressure difference caused by the pipe submergence depth may be comparable to the drywell pressurization, i.e. negligible gravitation may not be justified in the dimensional analysis. Fig. 16 shows drywell and wetwell gas pressures measured in the PPOOLEX experiment SLR-05-02, where air was blown into the drywell from air tanks. This caused the drywell to pressurize and air was injected through the vent pipe into the pool water. The first bubble appeared at the vent exit at about t = 1.5 s, i.e. roughly when the drywell pressurization exceeded the gravitational pressure difference since the drywell pressurization rate was quite slow. The gravitational pressure difference is $\Delta p = \rho g h$, where ρ, g and h are the water density, gravitational acceleration and pipe submergence depth, respectively, i.e. we have for the PPOOLEX facility $\Delta p \approx 0.1$ bar. It is easy to see that the scaling discussed above would not work at least for this particular experiment. By considering for instance a scaling factor of 3, for the linear time scaling $t \sim L$ the first bubble would be supposed to appear at $t = 3 \times 1.5 = 4.5$ s in the large scale. However, at this time the drywell over-pressure would be same as in the small scale at t = 1.5 s, i.e. only about 0.1 bar. The gravitational pressure difference in the large scale would be about 0.3 bar, which is much larger than the drywell pressurization and hence no vent clearing would occur at t = 4.5 s in the large scale.

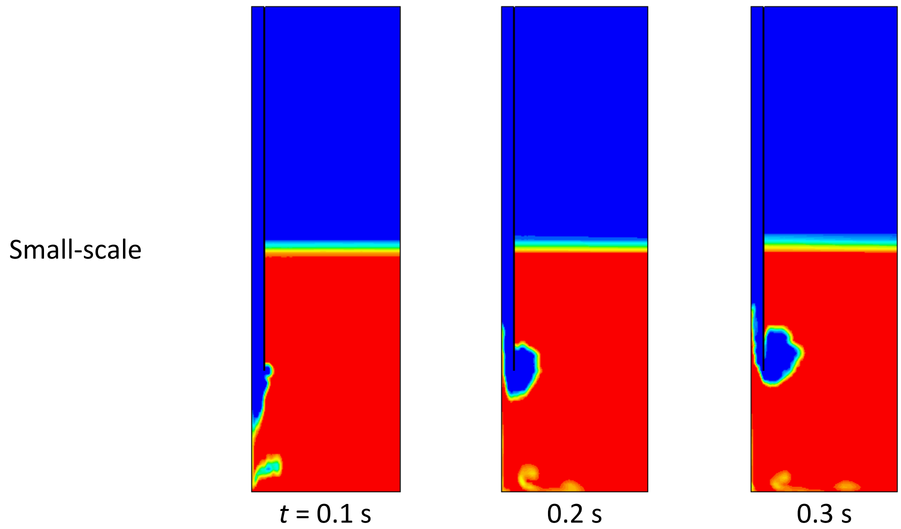

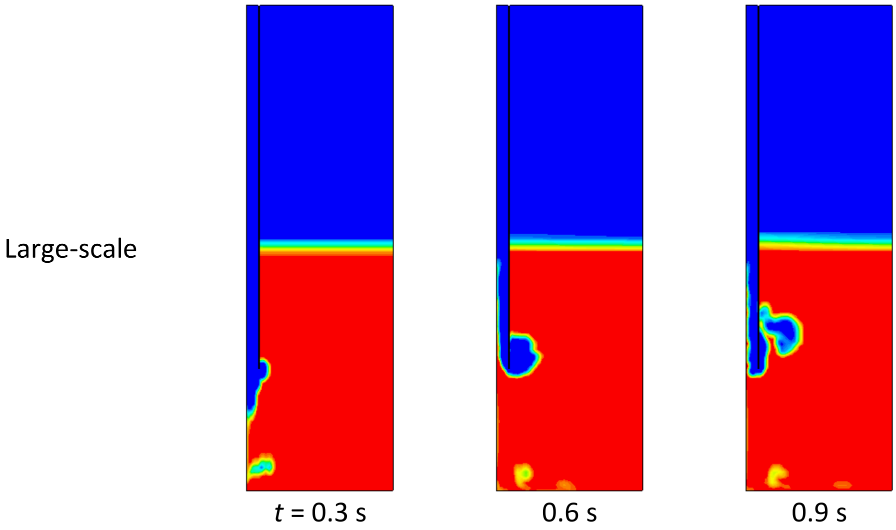

Figure 13. Comparison of bubbles for small and large scale at corresponding times using linear scaling t ~ L.

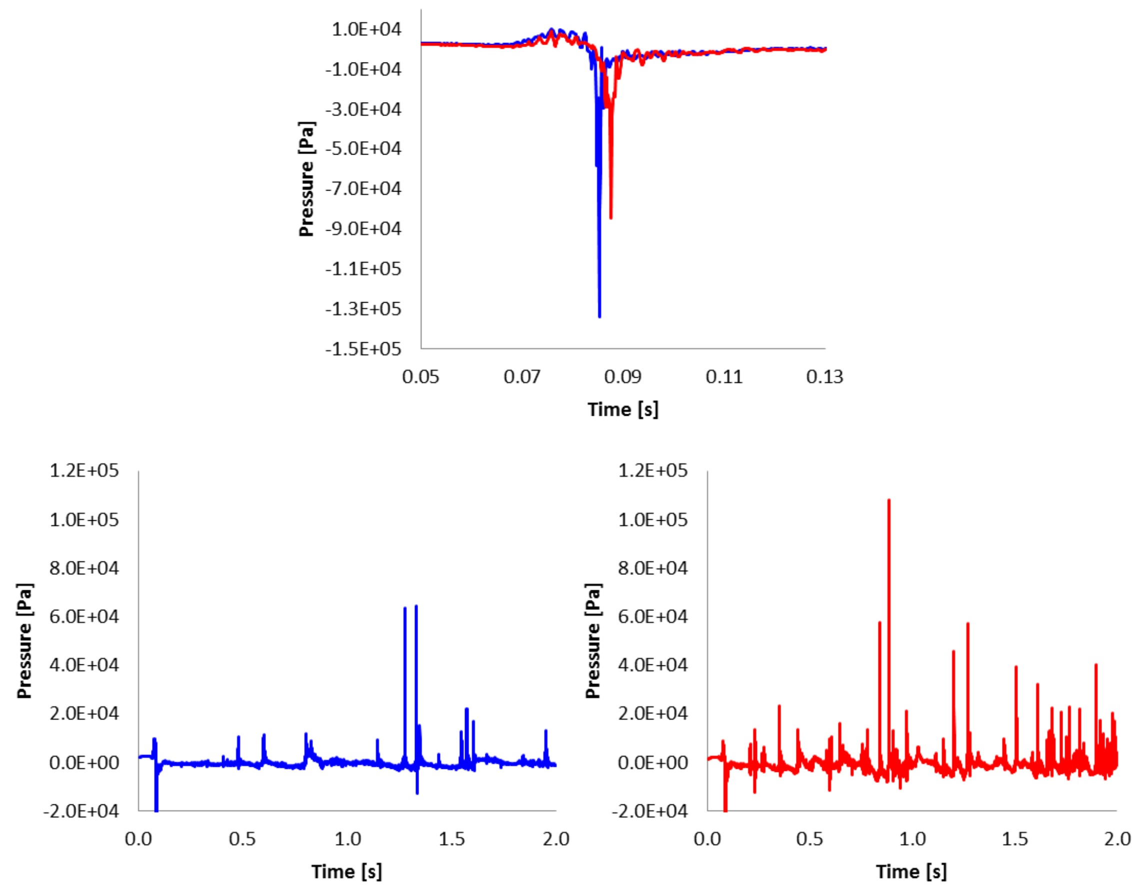

Figure 14. Pool bottom average pressure for small and large scale using linear scaling t ~ L. Time axes of small scale are shown. (— small scale, — large scale)

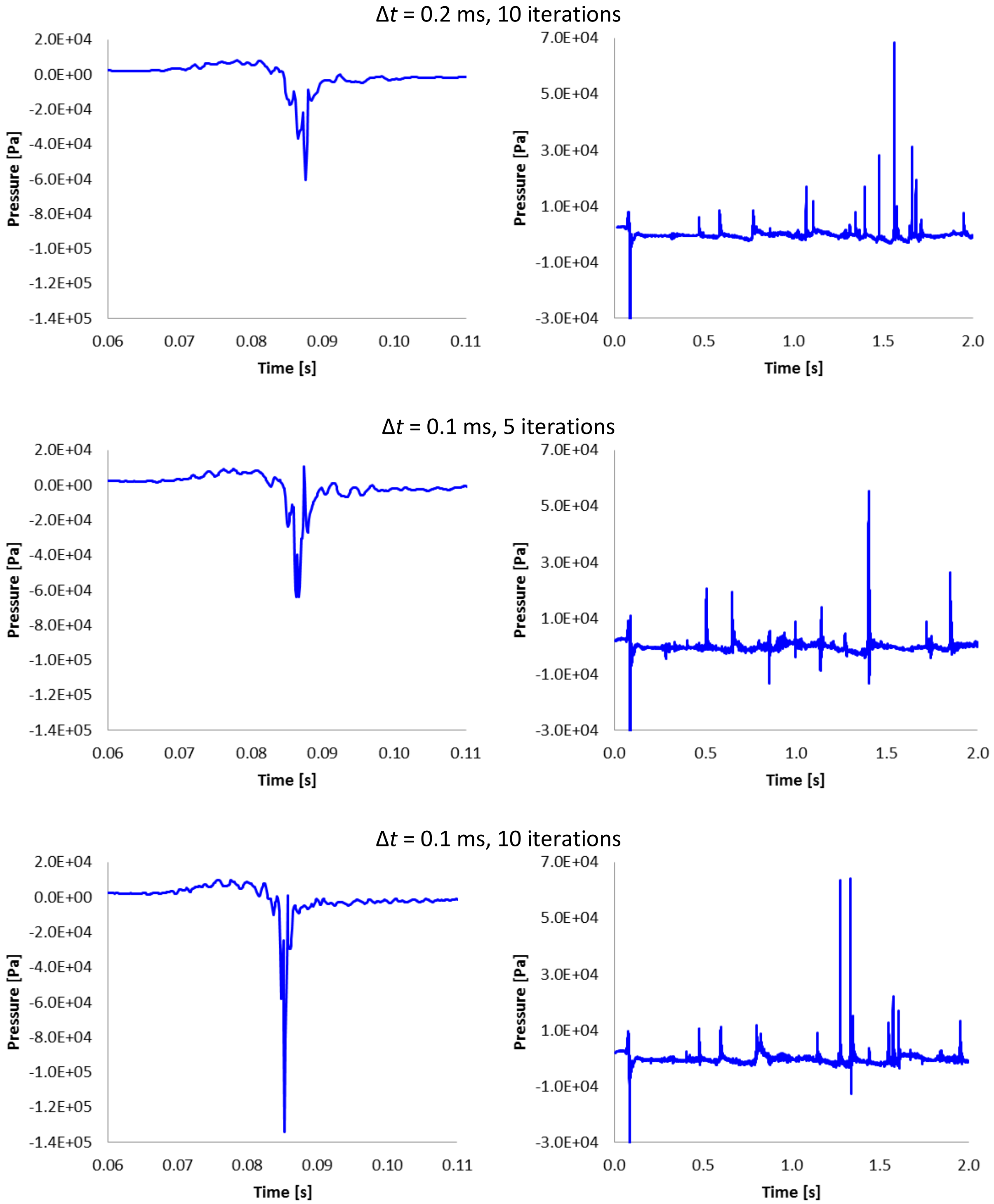

Figure 15. Pool bottom average pressure for small scale with different time steps and iterations inside time step. (Continues on the next page)

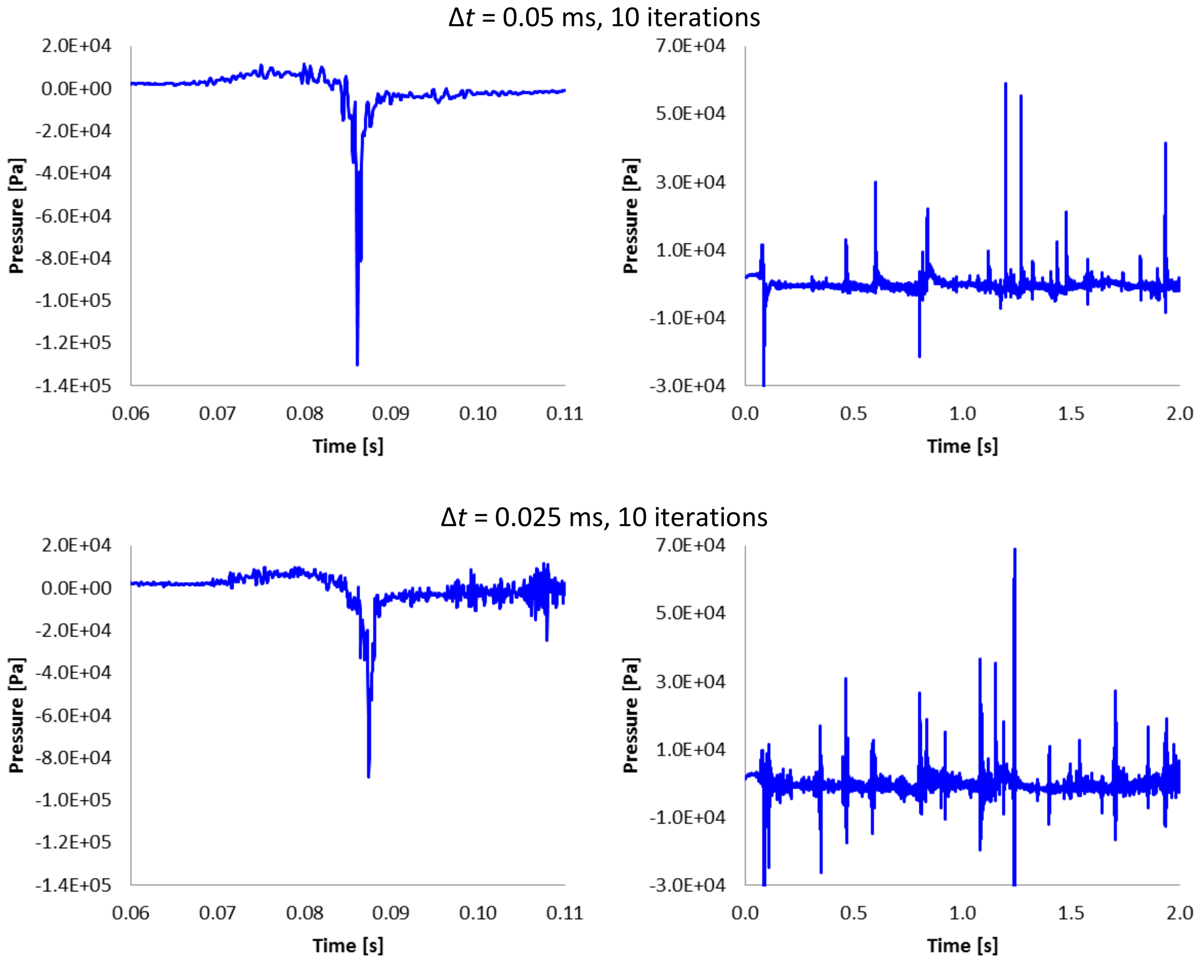

Figure 15. Continues from the previous page.

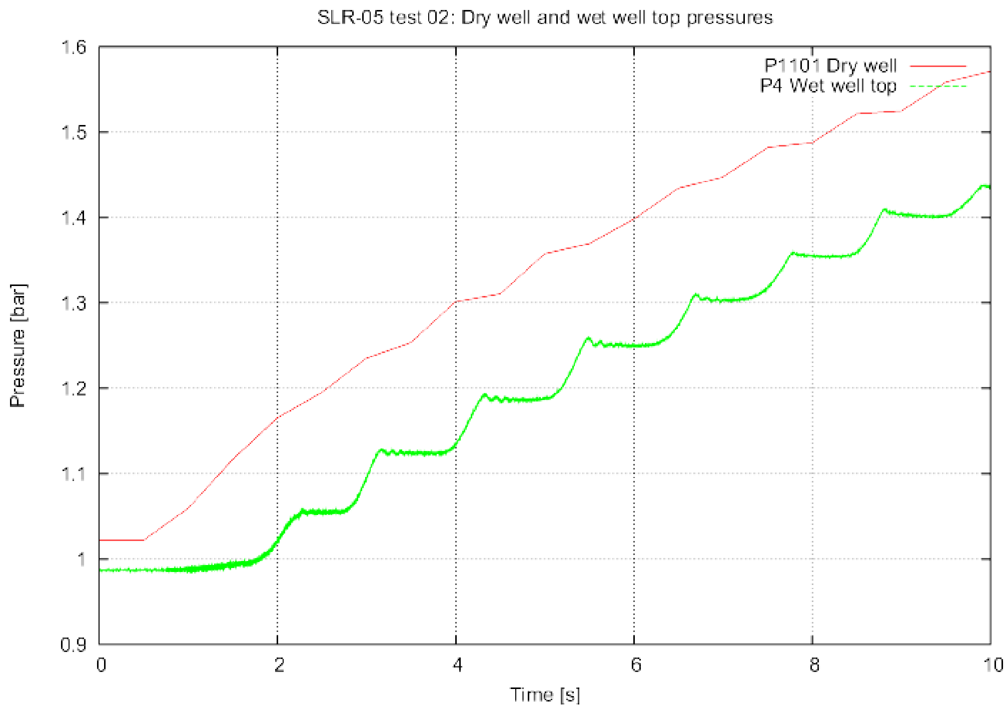

Figure 16. Measured drywell and wetwell pressures in PPOOLEX experiment SLR-05-02.

3.2 Water surface oscillation

3.2.1 Analytical model

The natural oscillation frequency of the water surface in the vent pipe has been studied with a simplified analytical model in Appendix A. Equation derived for the natural frequency is

$$f = \frac{1}{2\pi}\sqrt{\frac{\gamma A_1(p_1/V_1 + p_2/V_2) + \rho g(1 + A_1/A_2)}{\rho(H_1 + H_2 A_1/A_2)}} \tag{5}$$

where p_1 is drywell gas pressure, p_2 is wetwell gas pressure, V_1 is drywell gas volume, V_2 is wetwell gas volume, A_1 is area of water surface in the vent pipe, A_2 is area of water surface in the pool, H_1 is height of water column in the vent pipe, H_2 is height of water column in the pool above vent pipe exit, ρ is water density, γ is ratio of specific heats for air and g is acceleration of gravity. Values of the parameters for the PPOOLEX facility are listed in Table 2 for the stationary condition before blowdown.

During the chugging condensation, the water column is occasionally completely expulsed from the pipe, and occasionally sucked back some distance into the pipe. With complete expulsion of the water column from the pipe, the inertia term of the oscillation results mainly from the water mass near the pipe outlet. Below we analyse separately the case of water column in the pipe and the case of bubble at the pipe outlet.

Table 2. Parameters for the PPOOLEX facility in stationary condition before blowdown.

p_1 [bar]	p_2 [bar]	V_1 [m^3]	V_2 [m^3]	A_1 [m^2]	A_2 [m^2]	H_1 [m]	H_2 [m]	ρ [kg/m^3]	γ [-]	g [m/s^2]
1.0	1.0	13.54	9.1	0.0356	4.45	1.1	1.1	1000	1.4	9.81

3.2.1.1 Water column in the pipe

For the PPOOLEX facility, the ratio of the vent pipe and pool cross-section areas is $A_1/A_2 \approx 0.008$. Therefore, the terms involving A_1/A_2 may be neglected as small when H_1 and H_2 have same order of magnitude. In case of Eq. (5) this means that practically all of the pressure difference is involved in accelerating the water column in the vent pipe. The frequency may be simplified as

$$f = \frac{1}{2\pi}\sqrt{\frac{\gamma A_1(p_1/V_1 + p_2/V_2) + \rho g}{\rho H_1}} \tag{6}$$

The relative importance of the pressure and gravitational effects on the oscillation frequency can be found by observing the magnitudes of the spring terms of Eq. (6):

$$\gamma A_1(p_1/V_1 + p_2/V_2) \tag{7}$$

$$\rho g \tag{8}$$

Eq. (8) is about 9900 Pa/m. For the values in Table 2, Eq. (7) is about 900 Pa/m, which is negligible compared to the gravitational term. On the other hand, in the experiment COL-01, for instance, the pressures during chugging were about $p_1 = p_2 = 2.8\times10^5$ Pa, for which Eq. (7) is about 2600 Pa/m.

Thus, for moderate pressurization of the pool, the pressure term is here negligible and the natural frequency is governed by the gravitational effect, and Eq. (6) simplifies to

$$f = \frac{1}{2\pi}\sqrt{\frac{g}{H_1}} \tag{9}$$

We see that time scales as $t \sim \sqrt{L}$ when only the gravitational term Eq. (8) is significant. This is the same scaling result as for the gravity driven rise of large bubbles in the pool (Timperi et al., 2013). On the other hand, if only the pressure term Eq. (7) is significant, it is seen that time scales linearly as $t \sim L$, which is the same scaling result as for the discharge with gravitation neglected (Sonin, 1981; Timperi et al., 2013).

One also notes that the pressure term scales as $\sim 1/L$ while the gravitational term is independent of the system size, showing that the importance of the pressure term compared to the gravitational term decreases with increasing system size.

3.2.1.2 Bubble at the pipe outlet

When a bubble has formed at the pipe outlet, the natural frequency may be estimated by replacing A_1 with the surface area of the bubble and by using an effective length for H_1, which is of order the diameter of the bubble. In addition, the gravitational effect now results mainly only from the water column in the pool. The frequency is in this case approximately

$$f = \frac{1}{2\pi}\sqrt{\frac{\gamma A_1(p_1/V_1 + p_2/V_2) + \rho g A_1/A_2}{\rho(H_1 + H_2 A_1/A_2)}} \tag{10}$$

and the pressure and gravitational terms are

$$\gamma A_1\left(p_1/V_1 + p_2/V_2\right) \tag{11}$$

$$\rho g A_1/A_2 \tag{12}$$

By assuming, for instance, a bubble diameter twice the vent pipe diameter, an effective length of three times the bubble diameter (see Sec. 3.2.3) and pressures $p_1 \approx p_2 \approx 1\times10^5$ Pa, Eq. (11) and Eq. (12) are about 12000 and 1000 Pa/m, respectively. Thus, for this case the pressure term becomes significantly larger than the gravitational one.

3.2.2 CFD model

The axisymmetric model of the PPOOLEX facility is shown in Fig. 17. Here also the drywell has been included in the model. The dimensions are same as in the real facility, but the end sections of the pool have been approximated by straight walls. The volumes of water as well as of the drywell and wetwell gas volumes are approximately same as for the real facility. Due to the axisymmetry, the vent pipe has been modelled at the symmetry axis contrary to the real facility. Cell size near the vent pipe exit is 10 mm, while the maximum size in the wetwell water is 80 mm. In the wetwell and drywell gas, the maximum cell length is 200 mm.

The VOF model was used for the free-surface calculation and the standard *k*-*ε* model and wall functions were used for turbulence modelling, although the effect of turbulence is expected to be negligible in these simulations. Air was treated as compressible through the ideal gas law while water was assumed incompressible. Time step was 1 ms in the small-scale.

As discussed in Sec. 3.1.1, we use a scaling factor of 3 to obtain the large-scale pool model from the small-scale one.

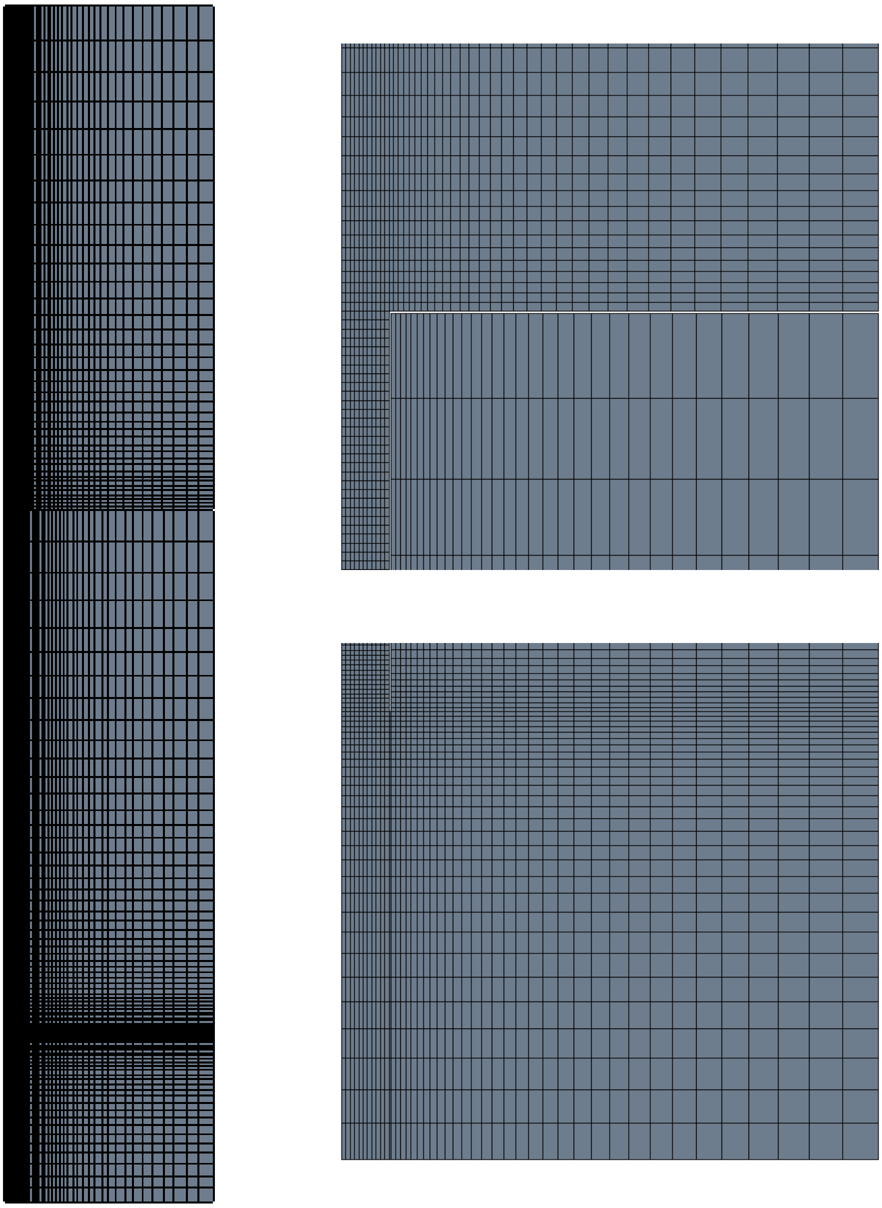

Figure 17. Axisymmetric CFD model including also drywell for the PPOOLEX facility. On the left: overall mesh, on the right: details of the mesh near drywell floor (top) and near wetwell floor (bottom).

3.2.3 Results

The natural frequencies obtained for different situations by using the analytical model and the CFD model are listed in Table 3 and Table 4. The locations of the water surfaces in the different cases are shown in Fig. 18.

For Case 1, Case 2 and Case 3, the additional effective length L_{eff} for H_1' was determined by comparing the analytical and CFD solutions for H_1 = 0.255 m, i.e. L_{eff} was set so that the same frequency results in the analytical and CFD solutions. In this case we find L_{eff} = 0.31D, where D is inner diameter of the vent pipe. This additional length results from the fact that there is a small region near the vent pipe outlet where the flow velocity in the pipe changes gradually to the flow velocity in the pool, as discussed in Appendix A and shown in Fig. 19. For Case 4 and Case 5, the effective length for H_1 was set to three times the bubble diameter; this value was obtained by matching the analytical results with the CFD results.

It is seen that the analytical and CFD results agree quite well. A better agreement is obtained expectedly for Case 1, Case 2 and Case 3 when the effective length is added to the height of the water column in the vent pipe.

Table 3. Natural frequencies [Hz] for Case 1, Case 2 and Case 3 (small-scale / large-scale).

Case	CFD	Analytical	
		$H_1' = H_1$	$H_1' = H_1 + 0.31D$*
Case 1	0.489 / 0.273	0.497 / 0.279	0.483 / 0.271
Case 2	0.242 / -	0.251 / 0.084	0.244 / 0.081
Case 3	0.913 / -	1.02 / 0.571	0.913 / 0.512

*An effective length of 0.31 × pipe diameter added due to small region near pipe exit where flow velocity in the pipe changes to flow velocity in the pool.

Table 4. Natural frequencies [Hz] for Case 4 and Case 5 (small-scale / large-scale).

Case	CFD	Analytical*
Case 4	1.53 / -	1.48 / 0.494
Case 5	1.69 / -	1.72 / 0.573

*An effective length of 3 × bubble diameter has been used for H_1.

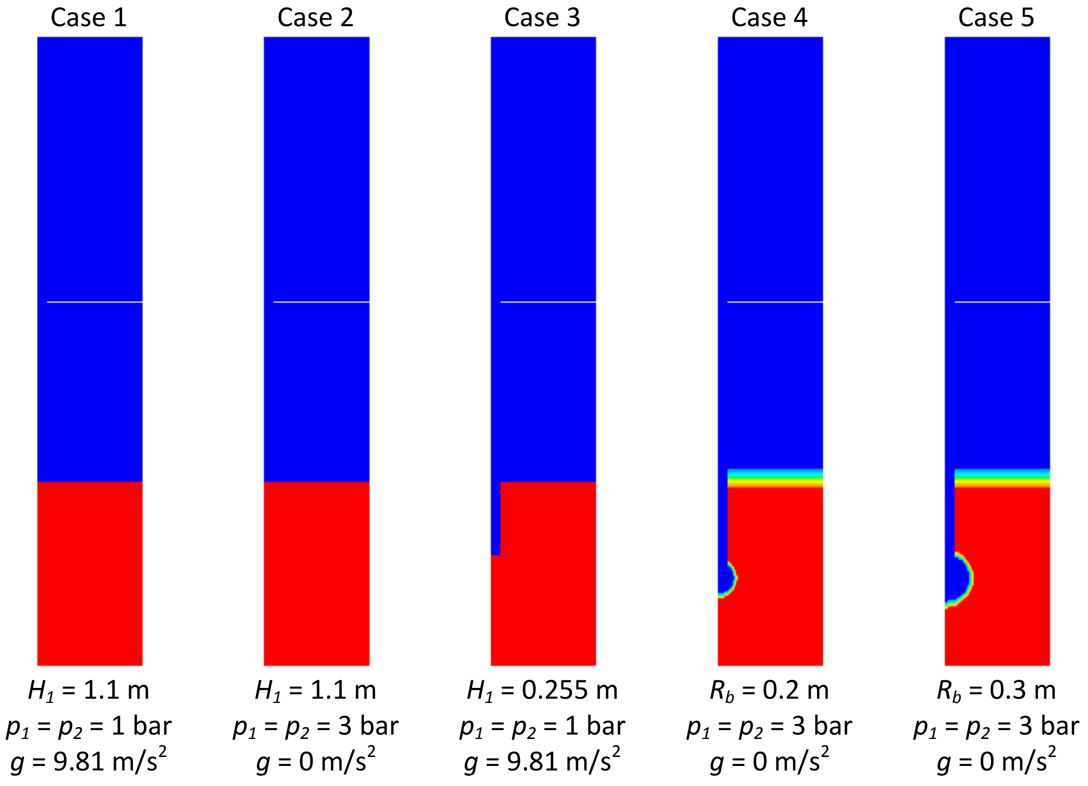

Figure 18. Oscillation cases modelled by axisymmetric CFD model of the PPOOLEX facility. The volume fraction of air and water is shown in blue and red, respectively.

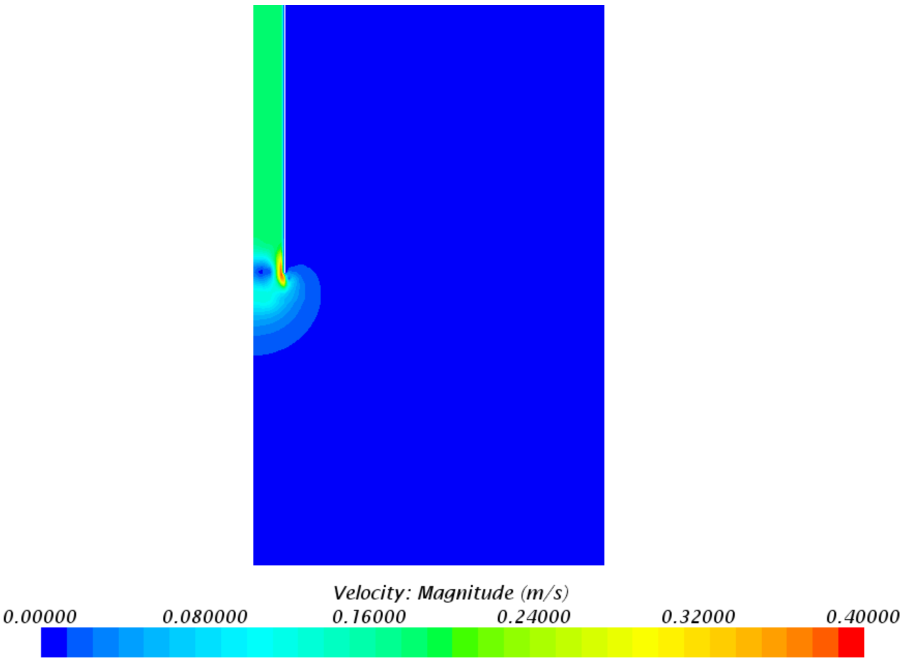

Figure 19. Velocity magnitude in the pool for oscillation in Case 1.

4. Simulation of BWR containment with acoustic FSI model

4.1 Mesh sensitivity studies

In order to verify that the used water mesh is adequately fine, i.e. the surrounding structure experiences an accurate loading caused by the pressure pulse, a mesh sensitivity study was performed for a sector model of the pool water. Both models are presented in Figure 20. The model with fine mesh consisted of 32 337 acoustic linear brick elements, whereas the model with coarse mesh consisted of 568 acoustic linear brick elements. In addition to number of elements, the shape of the pipe varied between the models; in the model with fine mesh, the cross-section of the vent pipe was circular. In order to reduce the number of elements, a square cross-section was used in the model with coarse mesh. The area of the cross-section was equal in both cases.

The top surface was assigned as free, i.e. the acoustic pressure is zero. All other surfaces were modelled as rigid walls. The acoustic pressure signals were compared from two corresponding locations of each model. The acoustic pressures at nodes 57 and 3 are presented in Figure 21 and the acoustic pressures at nodes 186 and 220 are presented in Figure 22. The results show that the magnitude of the first pressure peak is almost equal at both locations. The subsequent decrease in the peak values with the coarse mesh results from numerical damping and it is not assumed to affect significantly the stochastic FSI simulations where different loads are compared. Hence it was concluded that the coarse mesh can be used for the stochastic FSI computations.

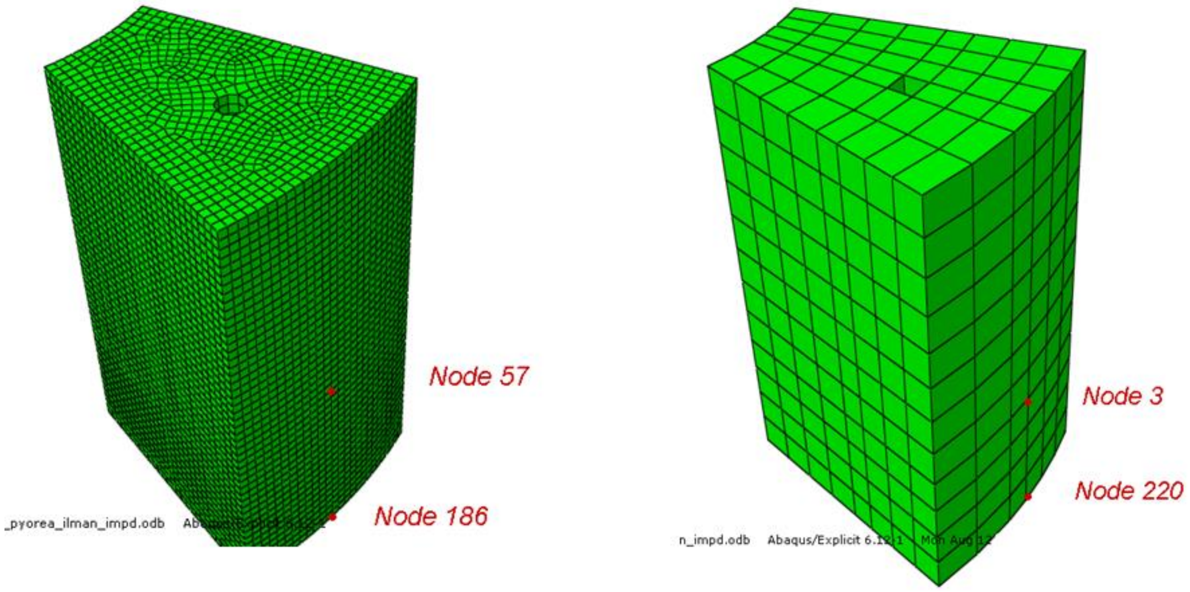

Figure 20. Models of a sector of BWR pool water with fine and coarse meshes.

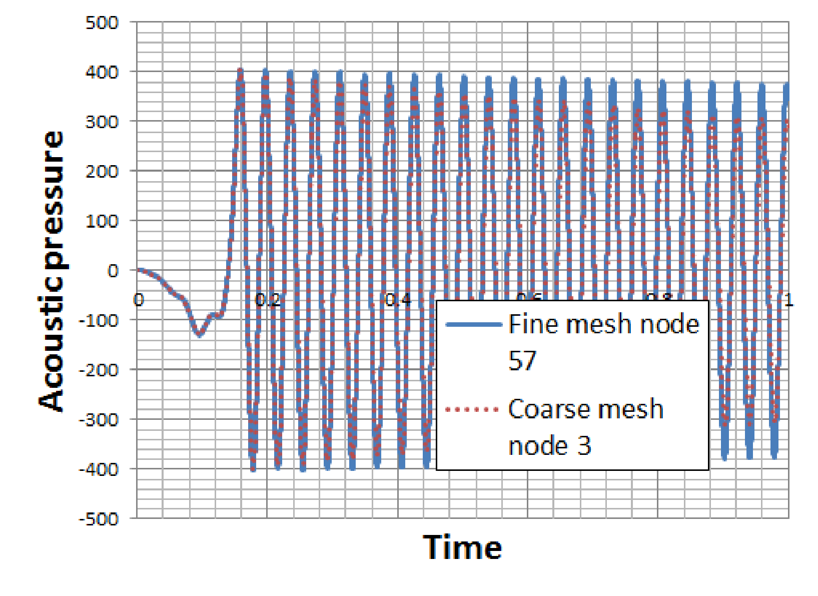

Figure 21. Acoustic pressure at node 57 (fine mesh) and node 3 (coarse mesh).

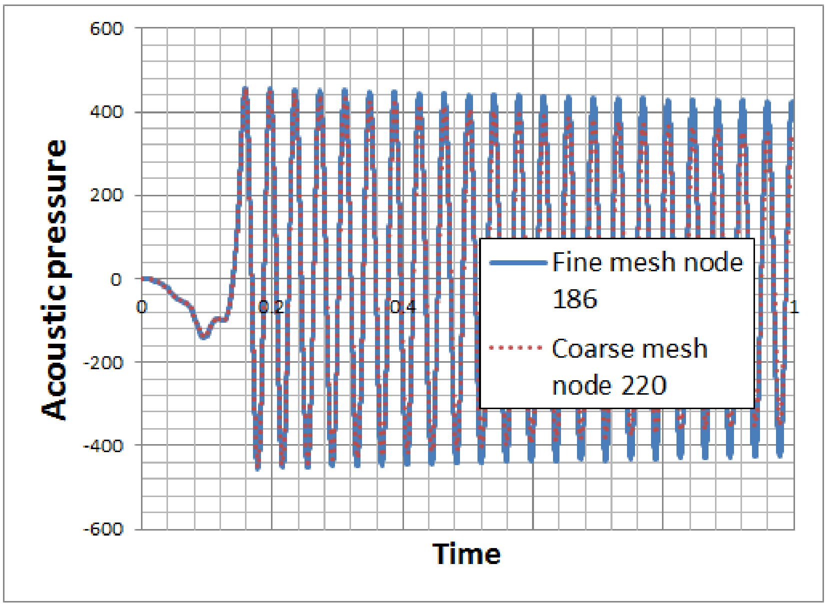

Figure 22. Acoustic pressure at nodes 186 (fine mesh) and node 220 (coarse mesh).

4.2 Convergence of statistics

Since the desynchronization time between chug events is not constant, the structural response was studied during multiple chug events, in which the desynchronization time varies. The desynchronization times were obtained by creating a normal distribution with mean value being zero and standard deviation 0.042 s. Out of this distribution, altogether 1600 initiation times (100 per pipe) were determined initially using Matlab's random-function, which gives randomly selected values out of a given distribution. The simulated time corresponding to 1600 chug events is roughly 206 seconds. In order to study whether the simulation time is sufficient or excessively long, the root-mean-squared (RMS) radial displacements from 835 locations (nodes) were determined from the results from periods 206, 106, 56 and 26 seconds. From the computed RMS values, the relation between RMS value corresponding to 206 seconds of simulated time and every other RMS value corresponding to less simulated time was computed.

The average, maximum and minimum values of relation between RMS values from time periods with varying lengths are presented in Table 5 and the RMS radial displacement at 10 randomly picked nodes from varying simulated time periods are presented in Figure 23. The average value is close to unity in each case, but the maximum and minimum values deviate more as the difference between the simulated time increases. Based on the computed relations between RMS displacements from 206 and 106 seconds of simulated time, it was concluded that the simulated time can be decreased to 106 seconds, i.e. 50 chug events per pipe.

Table 5. Average, maximum and minimum values of the relation between RMS values from time periods with varying length from 835 locations.

Value	RMS206/RMS106	RMS206/RMS56	RMS206/RMS26
Average	0.985	1.019	1.010
Max	1.025	1.145	1.273
Min	0.940	0.928	0.877

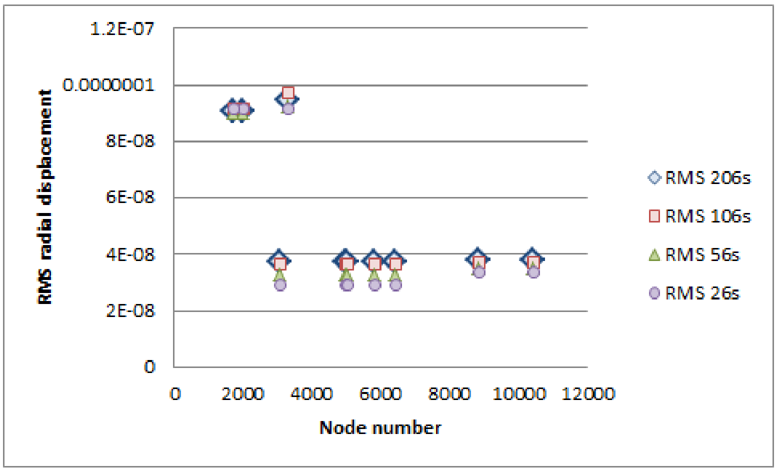

Figure 23. RMS radial displacement at 10 randomly picked nodes from simulated time of 206, 106, 56 and 26 seconds. Note that unit loading has been used, i.e. the magnitudes are not realistic.

4.3 Material damping

In the previous report by Timperi et al. (2013), it was concluded that the material damping of concrete has a significant effect on the structural response. Hence the damping was studied via un-damped structural response. In order to adjust the Rayleigh damping coefficients [see Eq. (3)], the radial displacements at the nodes presented in Figure 24 were transformed into frequency domain using Matlab's Fast Fourier Transform (FFT). Based on the containment eigenfrequencies, the new Rayleigh damping coefficients were fixed at 5 % of critical damping for 3 and 30 Hz. The previous and new coefficients are $\alpha = 5.89$, $\beta = 9.95\times10^{-5}$ and $\alpha = 1.71$, $\beta = 4.82\times10^{-4}$, respectively. The previous and new structural damping and containment eigenfrequencies are compared in Figure 25.

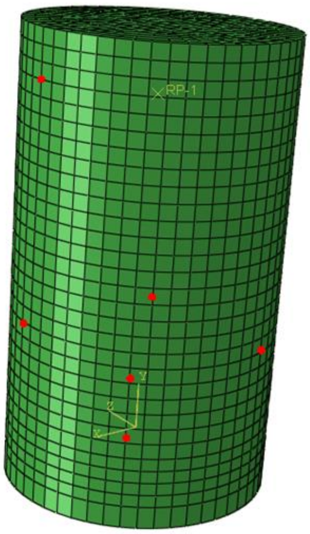

Figure 24. Locations of nodes from which radial displacement was transformed into frequency domain.

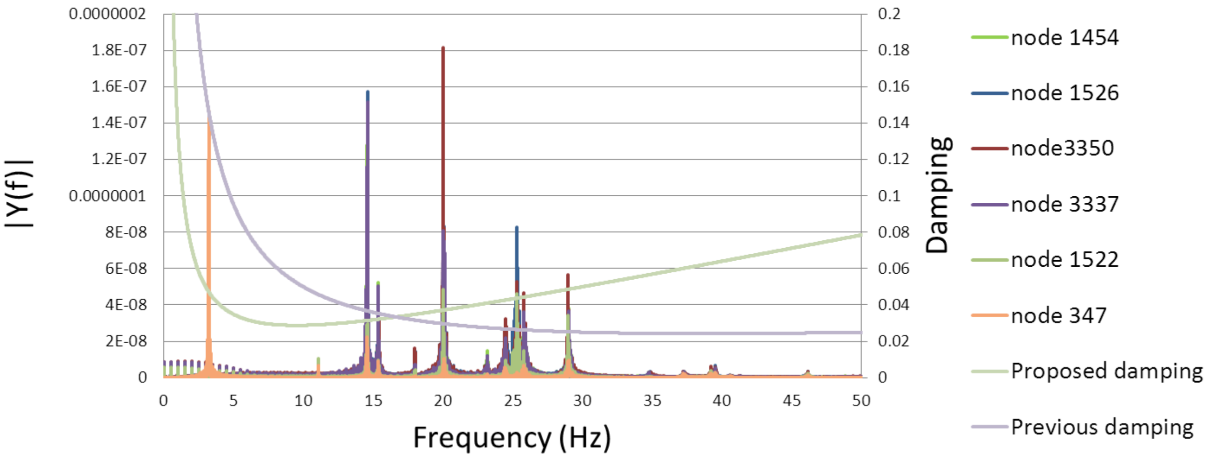

Figure 25. Comparison of previous and new structural damping and containment eigenfrequencies.

4.4 Load characterization

In the previous studies concerning FSI, the shape of the pressure pulse has been similar for each simulated chug event, taken as a representative chug event in PPOOLEX one-pipe experiment COL-01, with duration scaled to match that observed in large-scale tests presented by Kukita and Namatame (1985) (denoted Case 1 in the following). In the used pressure pulse, the magnitude of the peak pressure is clearly larger than that of the under-pressure. Pressure signal from two-pipe experiment PAR-10 is presented in Figure 26 and a magnification from a single chug event in Figure 27, where similar shape to that observed in COL-01 can be seen. The measured pressure signals in the large-scale experiment show a different kind of behaviour. The peak pressure is preceded by an under-pressure phase, which is often larger in magnitude than the peak pressure. In both cases, the duration of the under-pressure phase is longer.

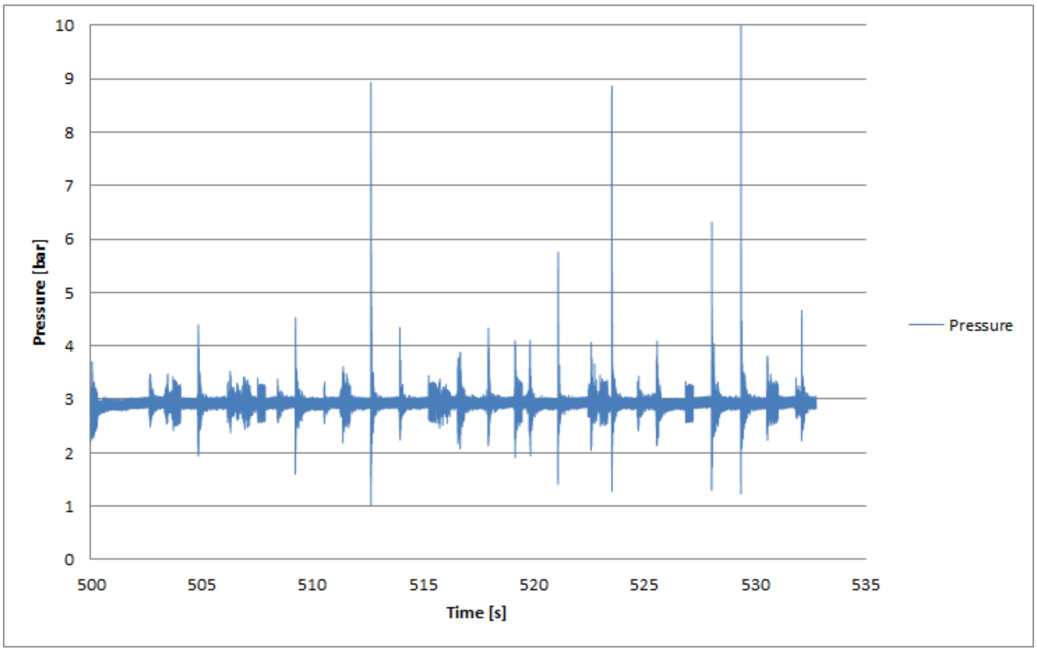

Figure 26. Pressure signal from PPOOLEX experiment PAR-10.

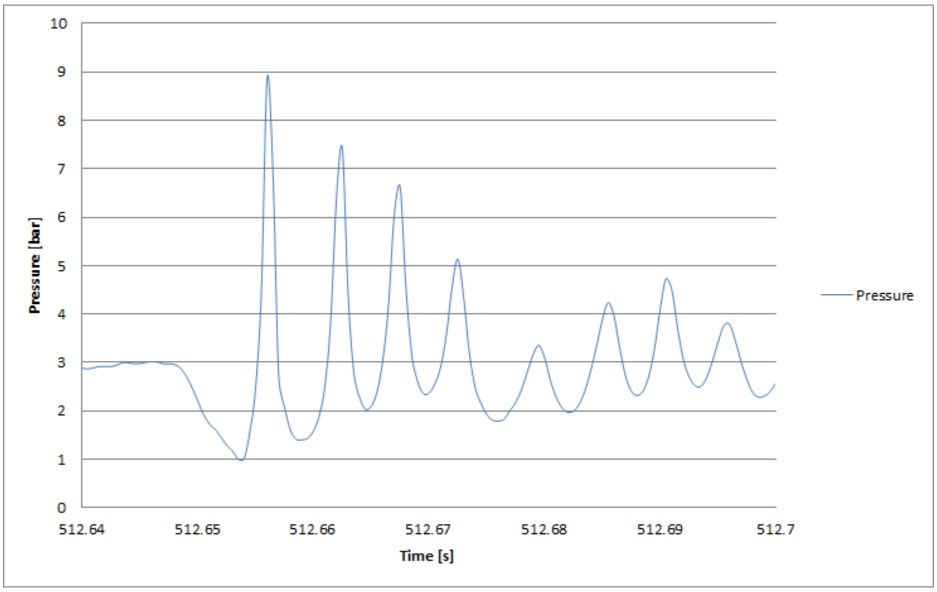

Figure 27. Magnification of a single pressure pulse from PPOOLEX experiment PAR-10.

In order to study the effect of the shape of the pressure pulse, an attempt was made to characterize the shape of the pressure signal in the seven-vent test (Kukita and Namatame, 1985). The characterization was performed with two different strategies. In the first approach (from now on referred to as Case 2), four average quantities were determined from seven measured pressure signals: the period between normal pressure and peak under-pressure, t_1, the magnitude of the peak under-pressure, h_1, the period from peak under-pressure to peak pressure, t_2 and the magnitude of peak pressure, h_2. Figure 28a presents the determined quantities in Case 2. According to the measured pressure signals of the large-scale tests, maximum amplitude occurs generally during under-pressure phase. The magnitude of the maximum amplitude used in the acoustic analyses is unity, which according to the measurements of the large-scale tests occurs during the peak under-pressure phase; the quantities h_1 and h_2 were utilized only to solve the relation between the peak under-pressure and peak pressure.

In the second approach (from now on referred to as Case 3), the shape of the pressure pulse were assumed to be symmetric, i.e. the duration of the peak under-pressure and peak pressure phase was determined as the average of the both phases. Figure 28b presents the determined quantities in Case 3. Typical expanded time histories of vent-outlet and pool-boundary pressures during a single chug event from the large-scale experiment are presented in Figure 29, from which the aforementioned quantities t_1, h_1, t_2, h_2 and t are determined. The pressure signal used in the previous analyses and those representing Case 2 and Case 3 are presented in Figure 30.

Case 2 pressure signal is utilized for studying the effect of the larger amplitude of peak under-pressure, whereas the simplified Case 3 signal is used for determining the importance of knowledge about the details of the loading.

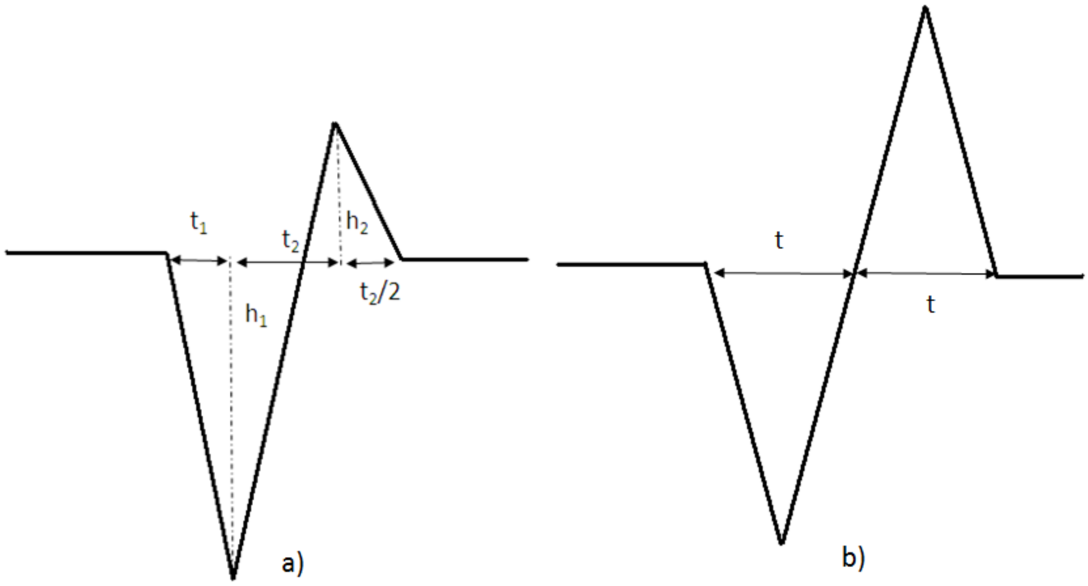

Figure 28. Determined quantities in Case 2 and Case 4 (a) and Case 3 (b).

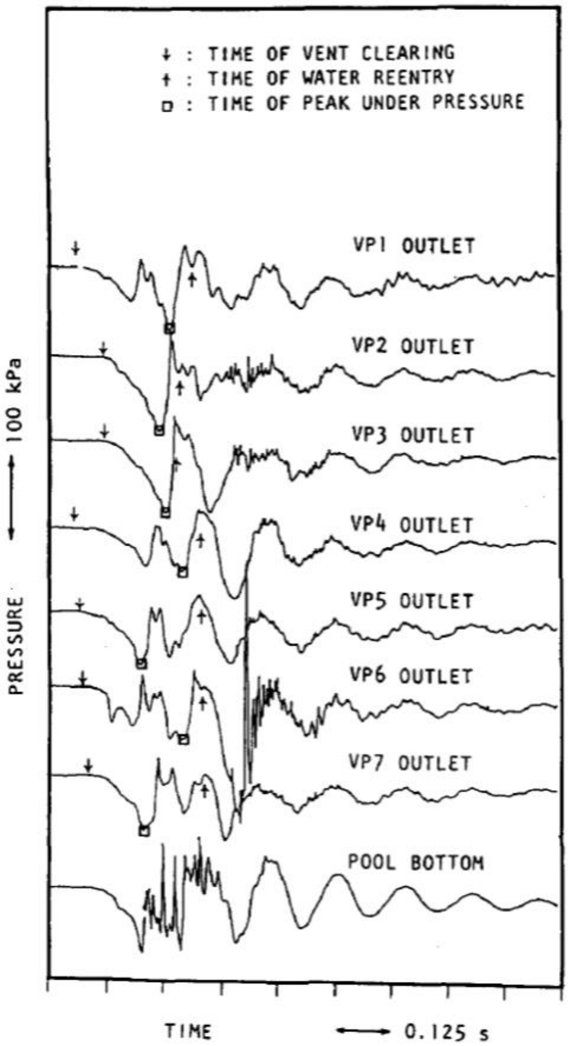

Figure 29. Pressure signals from large-scale (seven vent) experiment (Kukita and Namatame, 1985).

The determination of t_1, h_1, t_2, h_2 and t from the measured pressure signals requires some consideration. From Figure 29, one may conclude that the period between “normal pressure state” and peak under-pressure does not necessarily consist only of smoothly decreasing pressure, but might include some perturbation. In such case, the time of initiation was determined from the last point of time that the pressure was at “normal pressure level”, i.e. at the same level it is at the beginning of the measurement (left hand side in the figure). When determining the period between peak-under pressure and peak pressure, t_2, two approaches were selected. In Case 2, the period between those two events was determined as the time between peak under-pressure and the time of water reentry. In Case 4, the period between those two events was determined as the time between peak under-pressure and the first pressure peak. This was done due to the fact that at VP5 and VP7 outlets, there are pressure peaks between peak under-pressure and water reentry. When the period is determined as the time between the peak under-pressure and water reentry (Case 2), the averaged value (t_2) increases excessively and does not describe the more common behavior seen at other vent outlets, where the peak under-pressure is immediately followed by peak pressure (water reentry).

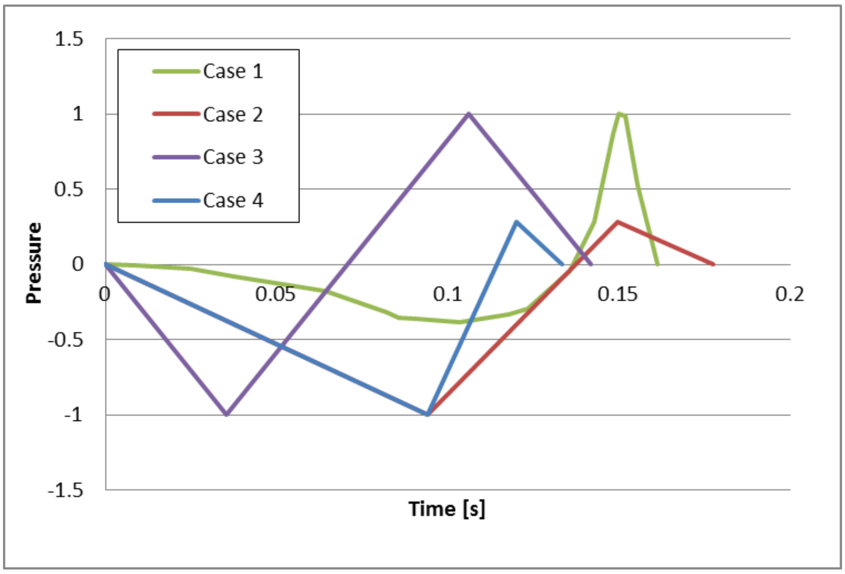

Figure 30. Normalized pressure signal from PPOOLEX COL-01 used in the previous analyses and simplified signals determined according to large-scale tests presented by Kukita and Namatame (1985).

4.5 Simulations with different load shapes

The simplified FEM model of the BWR containment including all 16 vent pipes is shown in Figure 31. The total number of elements is 21715, consisting of 8032 linear hexahedral acoustic elements (type AC3D8R in Abaqus), 1508 linear hexahedral continuum shell elements (type SC8R), 12173 linear hexahedral continuum elements (type C3D8R) and two mass elements. Explicit direct time integration was used for the solution. For the concrete structures, density was set to 2400 kg/m^3, elastic modulus to 39 GPa and Poisson's ratio to 0.17. The structural damping values described in Sec. 4.3 were applied. For water, density was set to 1000 kg/m^3 while sonic velocity was set to 450 or 1412 m/s based on Björndahl and Andersson (1998).

Average time between each chug event, the standard deviation of the desynchronization time and duration of a chug event were set same as in the previous study (Timperi et al., 2013), i.e 2 s, 42 ms and 150 ms, respectively. These values have been determined from the large-scale seven-vent pipe test with JAERI test facility presented by Kukita and Namatame (1985). For the sonic velocities 450 and 1412 m/s, the acoustic wave travels about 19 and 59 m, respectively, during the desynchronization time of 42 ms. Thus, the transit time for an acoustic wave through the pool water is quite short compared to the standard deviation of the desynchronization time, and it can be therefore expected that the desynchronization affects the pool behaviour. This was shown also in the previous study, where the desynchronization had quite significant effect.

The model and the loading desynchronization are described in more detail in the previous study (Timperi et al., 2013). Figure 32 shows node set from which statistics of horizontal displacement magnitudes were calculated and averaged over the nodes in order to compare the different loads.

Figure 33 shows deformations and stresses for the BWR containment simulation at selected instants of time for Case 1 loading. Generally the highest stresses are obtained at the lower parts of the inner and outer shell of the pool which are in contact with water.

Figure 34 and Figure 35 compare RMS and maximum horizontal displacement magnitudes for the different load cases using the water sonic velocities of 450 and 1412 m/s. Case 3 yields lowest RMS values while Case 4 lowest maximum values. However, differences between the load cases are relatively small, especially for the RMS values. The water sonic velocity seems to be a more important factor than the detailed load shape, namely clearly lower values are obtained with the higher sonic velocity. It should be noted, however, that here the sonic velocity is varied quite drastically. It is possible that the sonic velocity affects the eigenfrequencies of the pool so that with the lower sonic velocity the eigenfrequencies match better with the frequency of the load.

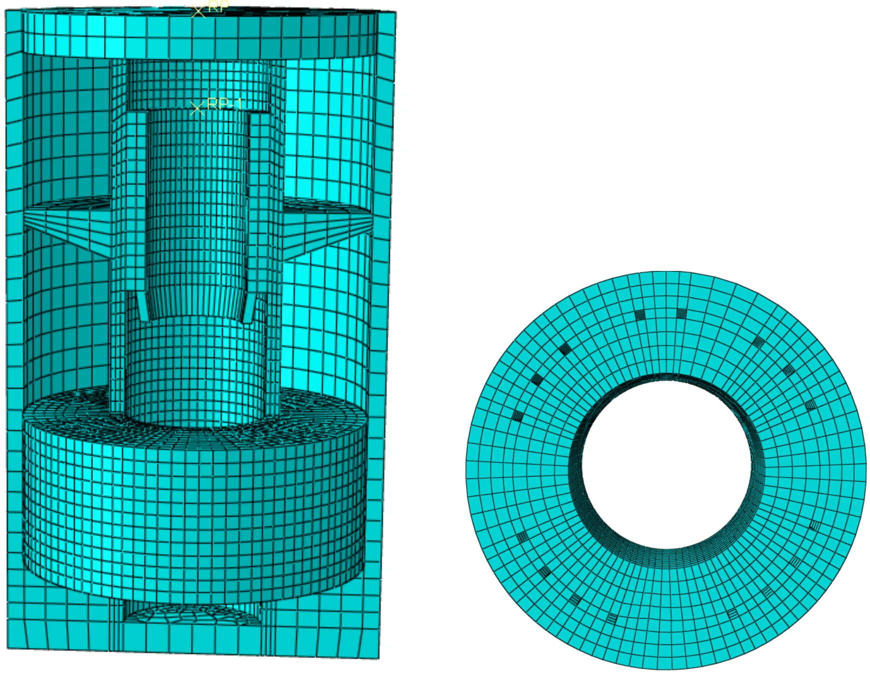

Figure 31. Simplified FEM model of BWR containment. On the left: model with part of concrete structures removed for visualization, on the right: wetwell water with simplified square shaped vent pipe cross-sections.

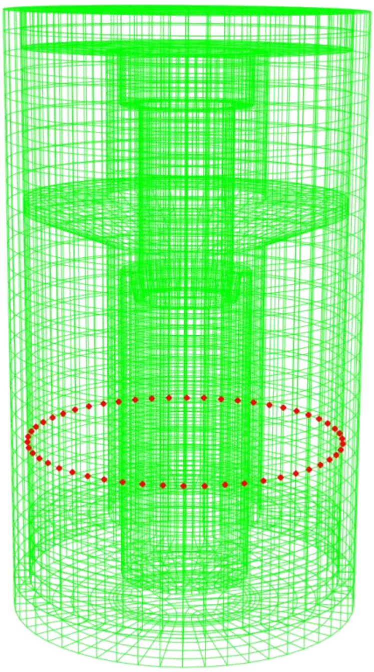

Figure 32. Node set at the inner surface of the outer containment shell for gathering displacement statistics.

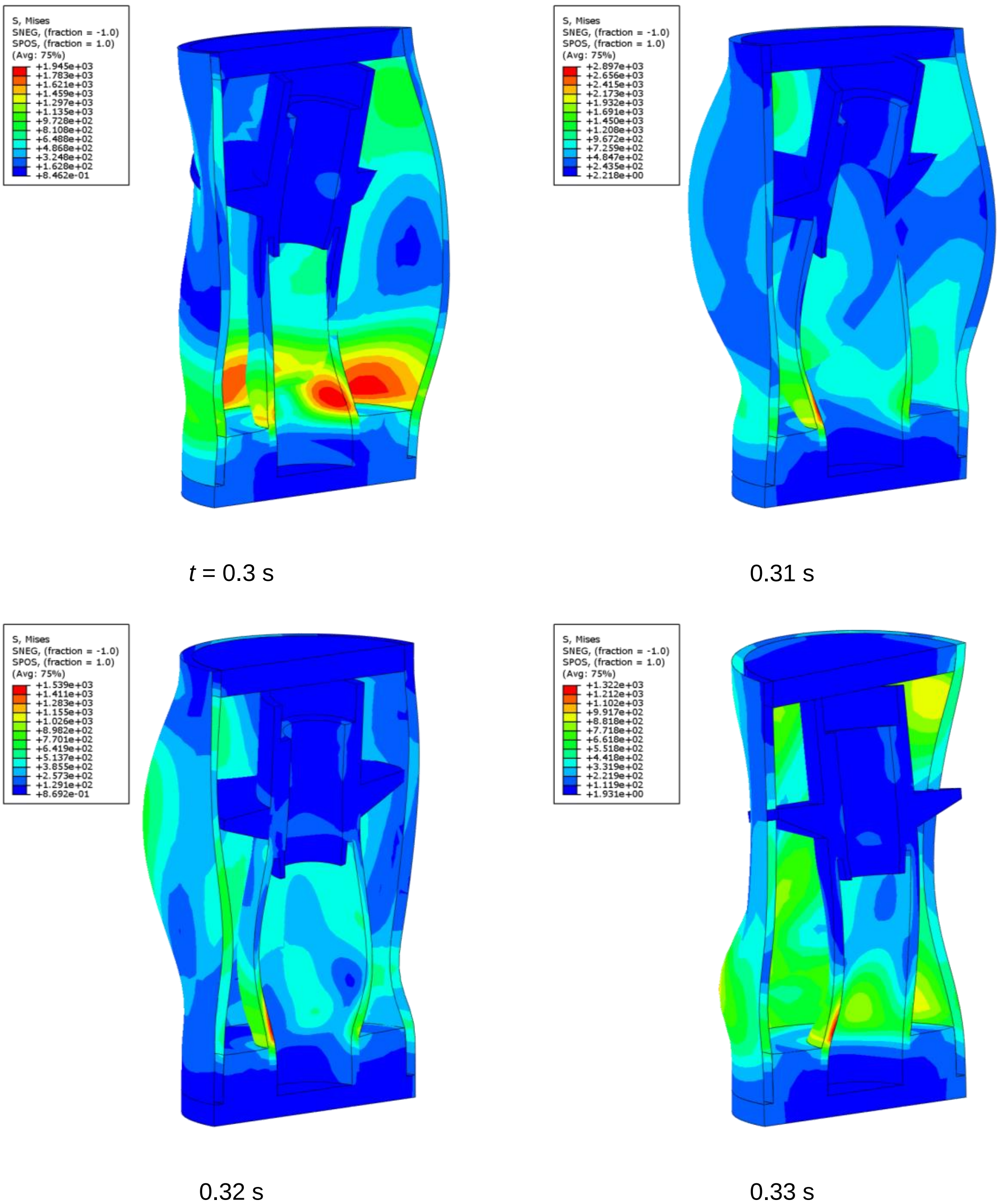

Figure 33. Deformations (scaled up by 7×10^6) and von Mises stresses (Pa) in the BWR containment for the acoustic FSI simulation with Case 1 load. Unit loading has been used, i.e. the magnitudes are not realistic. (Continues on the next page)

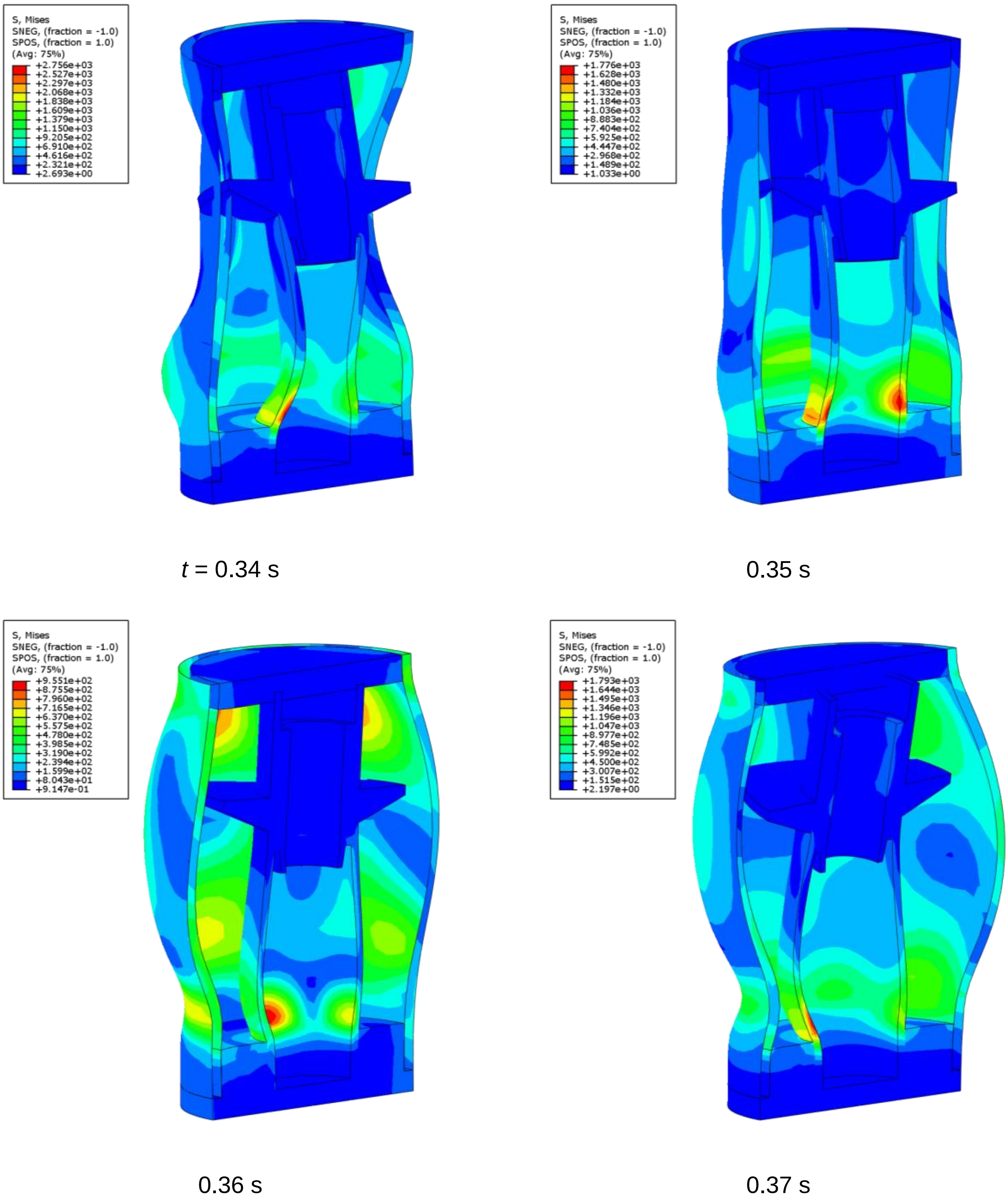

Figure 33. Continues from the previous page.

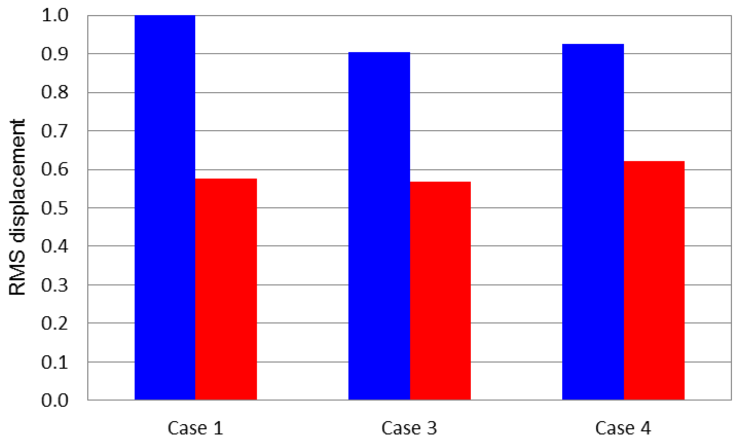

Figure 34. Normalized RMS horizontal displacement for different loadings. (■ c = 450 m/s, ■ c = 1412 m/s)

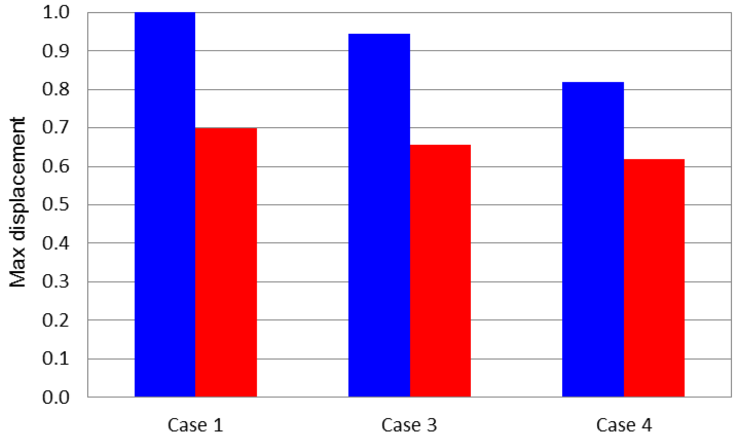

Figure 35. Normalized maximum horizontal displacement for different loadings. (■ c = 450 m/s, ■ c = 1412 m/s)

5. CFD modelling of direct-contact condensation

Two different approaches exist for solving two-phase flow of gas and liquid. In the Volume Of Fluid (VOF) model, the interface between the immiscible liquid and gas is tracked during the simulation. The interface is kept sharp with a numerical algorithm in order to reduce the effect of diffusion and to avoid mixing of the phases. In the Euler-Euler method, mixture of small gas bubbles and continuous liquid phase is considered, but the interface of the bubbles and the liquid is not solved in detail. Instead, the volume fraction of the bubbles in each grid cell is solved from so called two-fluid equations, where continuum approximation is used for the flow of small bubbles.

In modelling of the behaviour of large steam bubbles during blowdown of vapour into water pool, both tracking the surface of large bubbles and the volume fraction of small bubbles would be beneficial. Therefore, a hybrid method of VOF and Euler-Euler method would be useful, where the interfaces of large bubbles are tracked but only volume fraction of small bubbles is solved.

Laviéville (2008) and Coste (2013) have introduced the Large Interface Model, where “large” interfaces between the phases are resolved. In the following, the possibility of combining the Large Interface Model with the Euler-Euler model of ANSYS Fluent is discussed. The model equations are presented and their implementation by using the User-Defined Functions (UDFs) of Fluent are described.

5.1 Large Interface Model

5.1.1 Construction of the large interface

In the Large Interface Model, the first task is finding the location of “large interfaces” and “large bubbles”. This is done by calculating the surface area density vector $\bar{a}_P$ for each grid cell P:

$$\bar{a}_P = \frac{1}{V_P}\iiint_{V_P} \nabla\alpha \, dV = \frac{1}{V_P}\iint_{\partial V_P} \alpha \, d\bar{a} = \frac{1}{V_P}\sum\nolimits_f \alpha_f \bar{n}_f \tag{13}$$

Here, V_P is the volume of cell P, α is the liquid volume fraction, α_f is the liquid volume fraction at the cell face f and $\bar{n}_f$ is the outward pointing surface area vector of face f.

In the construction of the large interface, the grid cells with large surface area density are located. The first criterion for an interface cell is that

$$\bar{a}_{P_i} > \frac{1}{r_1}\bar{S}_{P_i} \ , i = x, y, z \tag{14}$$

is valid at least for one component of the surface area density vector. The maximum area density is depicted by

$$\bar{S}_{P_i} = \frac{1}{2}\sum\nolimits_f \left|\bar{n}_{f_i}\right| \ , i = x, y, z \tag{15}$$

and the parameter $r_1 = 5$.

In addition, a second criterion is used for the interface cell in the “surface thinning phase”. When adjacent cells both belong to the interface and are roughly parallel to the normal of the large interface, the cell with lower liquid fraction is removed from the surface. The condition for being parallel to the normal of the interface is

$$|(\bar{a}_P + \bar{a}_N) \cdot \bar{R}_{PN}| > r_2 \|\bar{a}_P + \bar{a}_N\| \|\bar{R}_{PN}\| \quad (16)$$

where the parameter is $r_2 = 0.7$.

When the large interface location and the normal of the interface are known, one can calculate the distances from free surface to gas and liquid cells near the surface. The three-cell stencil of the large interface is illustrated in Figure 36.

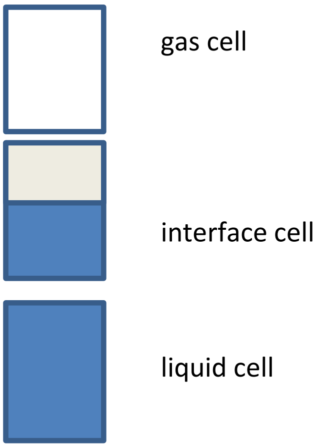

Figure 36. A three-cell stencil for describing interface of the phases in the Large Interface Model.

5.1.2 Heat transfer on the large interface

A model for the heat transfer on the large interface has been presented by Coste et al. (2008) and by Coste (2013). The gas phase sees the interface of the phases approximately similar to a solid wall. Therefore, standard wall functions have been applied to describe the boundary layer on the gas side.

The heat transfer coefficient on the liquid side is more complicated. The model for the heat transfer coefficient depends on whether the turbulence is weak or strong. In addition, three different models are used depending on the dimensionless distance between the interface and the center of the adjacent grid cell, $y_{le}^+ = y_{le} u' / v_{\mathrm{liq}}$. The velocity fluctuation u' is calculated from the turbulence kinetic energy: $u' = \sqrt{2k/3}$ and v_{liq} is the kinematic viscosity of the liquid.

The liquid side heat transfer coefficient is

$$h_{le} = \frac{\rho c_P u'}{T^+} \quad (17)$$

where T^+ is the dimensionless temperature difference between the interface and the center of the adjacent grid cell.

If the distance from the interface is small ($y_{le}^+ \leq \mathrm{Re}_{\mathrm{t}}^{1/4} \mathrm{Pr}^{-1/2}$), the model for the sublayer region is used, where the temperature difference depends linearly from the distance to the interface:

$$T^+ = \mathrm{Pr}\, y_{le}^+ \quad (18)$$

Here Pr is the Prandtl number and the turbulent Reynolds number is $\mathrm{Re_t} = 2u'L_\mathrm{t}/v_\mathrm{liq}$ and L_t is the length scale of turbulence.

In the logarithmic region ($\mathrm{Re_t^{1/4}Pr^{-1/2}} \leq y_{le}^{+} \leq 10\mathrm{Re_t^{1/2}}$), the temperature difference is

$$T^{+} = A\ \ln(y_{le}^{+}) + B \tag{19}$$

where

$$A = \frac{{}^{1}\!/_{K^{+}} - \mathrm{Re_t^{1/4}\,Pr^{1/2}}}{\ln\left(10\ \mathrm{Re_t^{1/4}\,Pr^{1/2}}\right)} \tag{20}$$

$$B = \frac{1}{K^{+}} - A\ \ln\left(10\ \mathrm{Re_t^{1/2}}\right) \tag{21}$$

Far away from the interface ($10\mathrm{Re_t^{1/2}} \leq y_{le}^{+}$), the temperature difference is

$$T^{+} = \frac{1}{K^{+}} \tag{22}$$

In the case of weak turbulence, we use (Coste, 2013) estimate

$$K^{+} = 0.35\ \mathrm{Pr^{-1/2}\ Re_t^{-1/2}}\left[0.3\ \left(2.83\mathrm{Re_t^{-3/4}} - 2.14\ \mathrm{Re_t^{-2/3}}\right)\right]^{-1/4} \tag{23}$$

For strong turbulence, we have

$$K^{+} = \mathrm{Pr^{-1/2}Re_t^{-1/8}} \tag{24}$$

The condition of weak or strong turbulence is determined by estimating the blob size as shown by Coste (2013). The blobs are moderately coherent and discrete volumes of fluid.

The large scale interface model described above was implemented in the ANSYS Fluent 15.0 CFD code by using User-Defined Functions (UDFs). In the following, the large scale interface method is applied to calculation of the experiment MIX-03 performed by Puustinen et al. (2012) with the PPOOLEX test facility. In this experiment, vapour is blown into a water pool. The interface of the large bubble at the outlet of the vent pipe is tracked by using the large scale interface model.

5.2 CFD model for PPOOLEX experiments

The PPOOLEX facility is a pressurized cylindrical vessel with a height of 7.45 meters and a diameter of 2.4 meters. The volume of the drywell compartment is 13.3 m^3 and the volume of the wetwell compartment is 17.8 m^3. Steam is blown into the drywell compartment via a horizontal DN200 inlet plenum. The experimental facility has earlier been described in detail by Puustinen, Laine and Räsänen (2010).

In the MIX-03 experiment, stratification of the water pool was studied. In order to achieve stratification, a small flow rate of vapor was first injected through the drywell and vent pipe into the water pool. At a later stage, the flow rate of vapor was increased, so that mixing of the water pool was achieved. At this stage, chugging in the vent pipe started at time t = 2 300 s. In the following, we concentrate on this chugging stage of the experiment. Specifically, we study the phenomena at time t = 2 600 s, when the conditions were fairly stationary.

The CFD calculation was carefully initialized to correspond to the situation at time t = 2 600 s. It was assumed that the amount of non-condensable gas in the drywell was very small because almost all air had already been blown to the wetwell. The mole fraction of air in the drywell was assumed to be 0.01 %. The temperature of the gas in the drywell was 129 °C. Since the drywell was insulated, the walls were initialized to the same temperature. The pressure in the drywell was p_{DW} = 2.70 bars. The temperature of the water pool was 27.5 °C, and the temperature of the gas space of the wetwell was about 50 °C.

The mass flow rate of vapor from the inlet plenum to the drywell was 0.432 kg/s and it was kept constant during the calculation. The temperature of the vapor was 142 °C and it contained a mass fraction of 0.01% of air.

The CFD calculations were performed by using the Euler-Euler two-phase model of ANSYS Fluent 15.0. The Euler-Euler model is a two-fluid model, where conservation of mass, momentum and energy are solved for gas and liquid water. The gas phase consisted of two species components: dry air and vapor.

The mass fraction of non-condensable gas flowing into the drywell was reduced from only 0.01 %. This means that in the drywell, the gas was almost pure vapor. The mixture of gases was modeled as an ideal gas. In the wall condensation and direct-contact condensation, the partial pressure model implemented earlier was applied, but some technical refinements that earlier limited the amount of direct-contact condensation were mitigated. The Hughes–Duffey model was used for heat transfer on the liquid side (Timperi et al., 2012).

5.3 Simulations with the Large Scale Interface model

When the pressure in the drywell compartment increases, water is blown out from the vent pipe. In Fig. 27, the mass flow rate in the top part of the vent pipe is shown. After clearance of the vent pipe, periodic formation of vapour bubbles at the outlet of the vent pipe starts. This phenomena can be seen as periodic oscillation in the mass flow rate through the vent pipe.

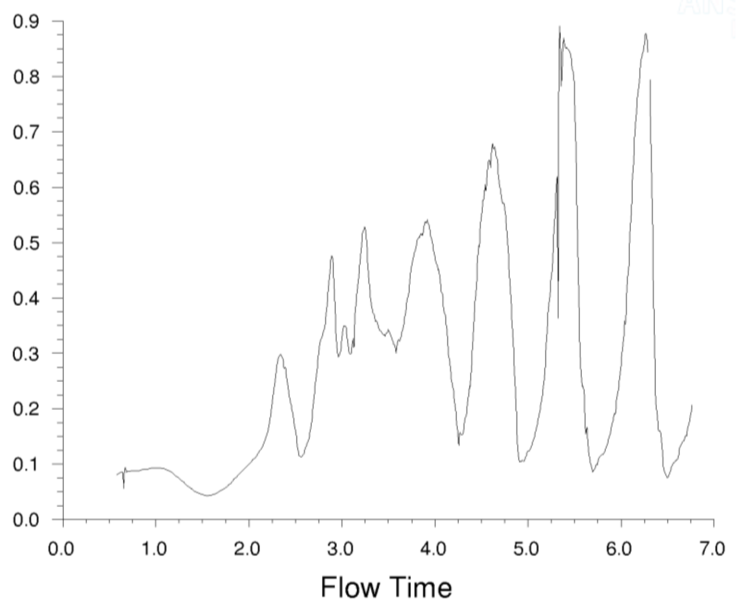

Figure 37. Mass flow rate flowing into the vent pipe.

The formation and condensation of one bubble is shown in Fig. 38, where the volume fraction of vapour is shown at different instants of time. At time t = 5.925 s, formation of a vapour bubble is starting and the interface between vapour and liquid water starts moving out from the vent pipe. At time t = 6.225 s, a large vapour bubble has formed at the outlet of the vent. The bubble is only partly condensed at the outlet of the vent pipe; a fraction of the vapour rises upwards and is condensed before it reaches water surface. Later, the interface between vapour and liquid water moves inside the vent pipe. Then, formation of a new bubble starts.

In Fig. 39, the results from locating the large scale interface between the phases is shown. The three-cell stencil at the interface between gas and liquid water is shown. The grid cell at the interface (yellow), the grid cell on the liquid side (red) and the grid cell on the gas side (cyan) are shown. The interface tracking algorithm is able to locate the bubble and the water level of the pool at almost every location, where large surface exists. At a few locations, however, gaps can be seen in the tracking results, which do not exist in the simulation result shown in Fig. 38.

In Fig. 40, the condensation rate at the large scale interface is shown at few instants of time. The condensation rate is smaller than in the experiment MIX-03, and therefore the period between the formation of bubbles is shorter than in the experiment. The liquid water penetrates into the vent pipe a shorter distance than in the experiment.

The implemented large scale interface model contains the basic functionality for the tracking of the large scale interfaces between gas and liquid. Improvements are, however, still needed in the modelling in order to achieve quantitatively satisfactory results. In particular, the validation of the “blob” size model needs to be performed. The stability of the implemented model also needs some improvements.

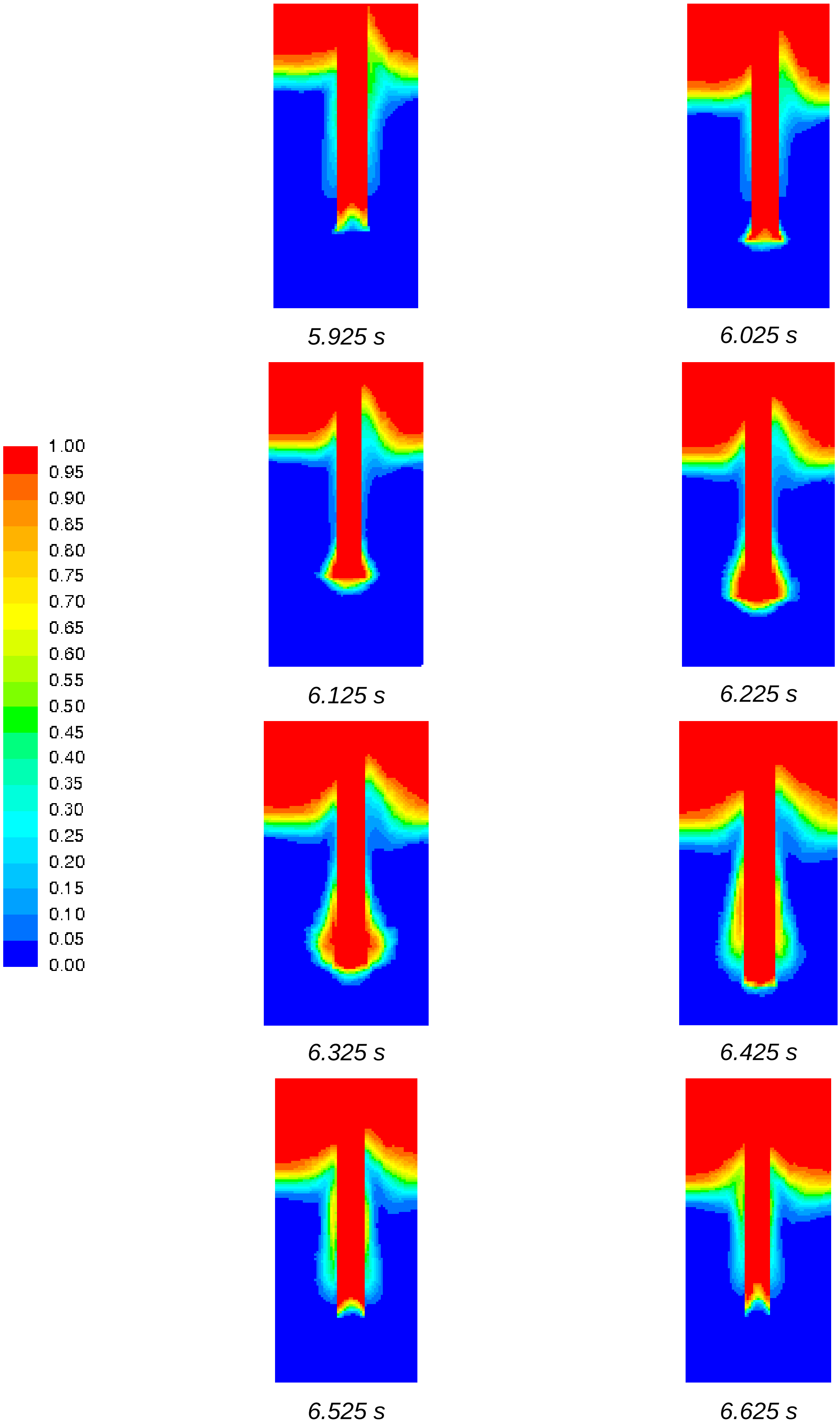

Figure 38. Volume fraction of gas at different instants of time during formation and condensation of a vapor bubble at the outlet of the vent pipe.

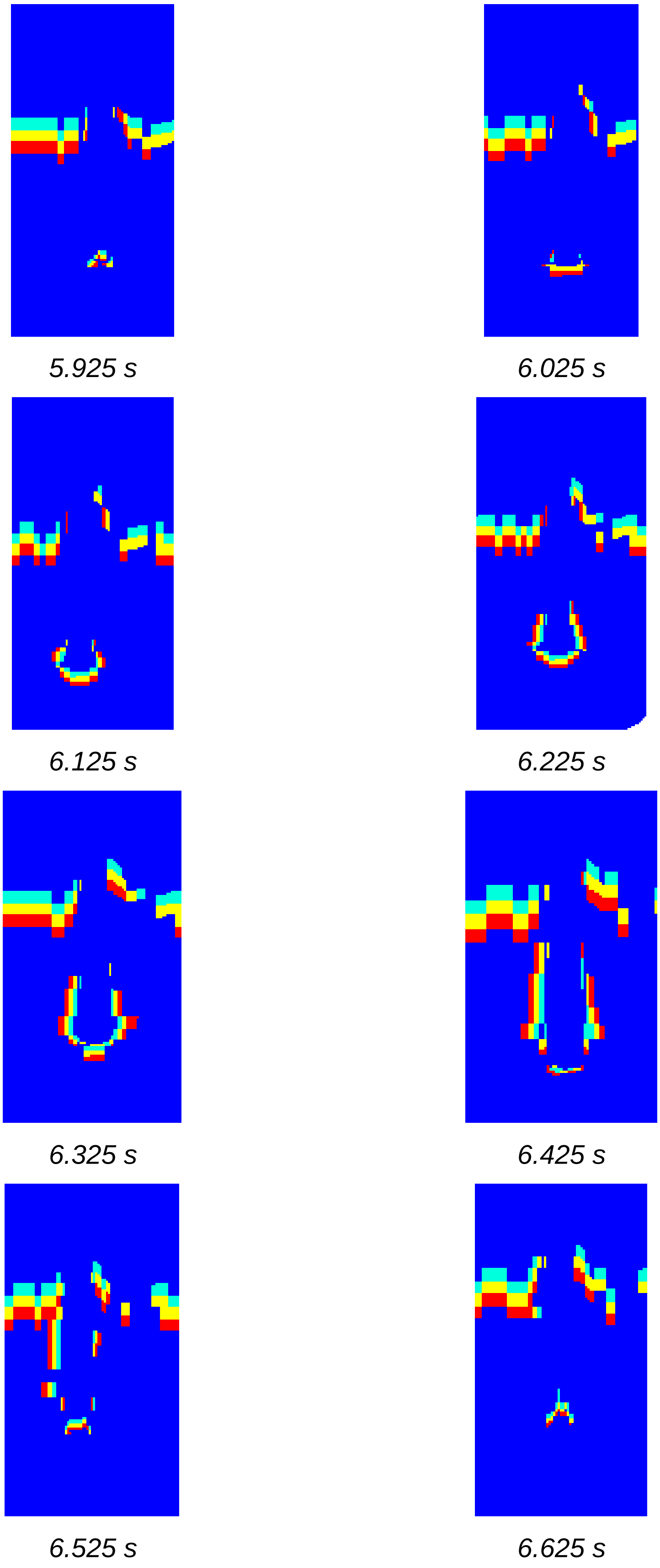

Figure 39. Large scale interface between the liquid and vapor phase. Determination of the three-cell stencil at the interface between the phases: liquid (red), interface (yellow) and vapor cell (cyan).

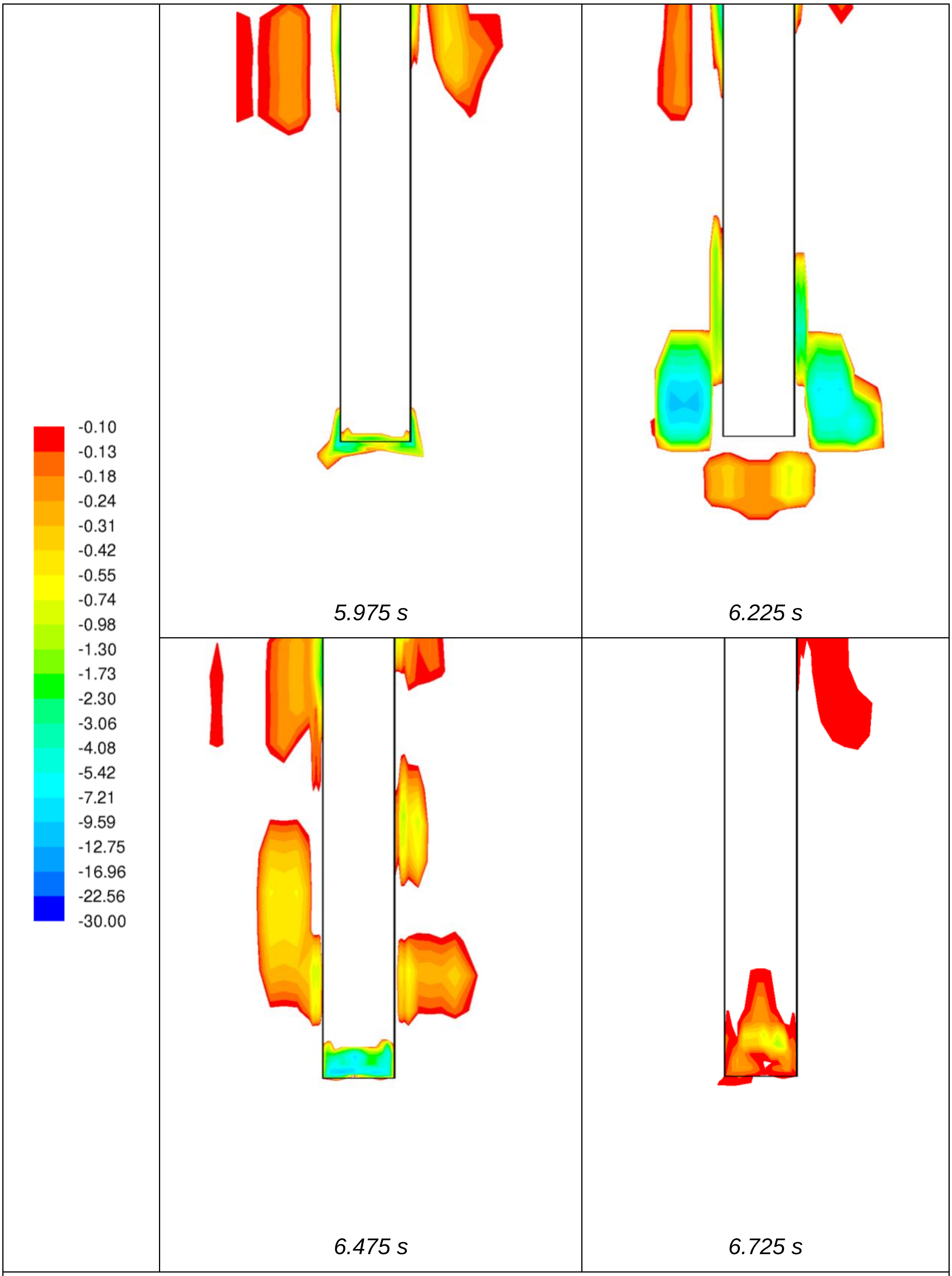

Figure 40. Condensation rate (kg/sm^3) at the large scale interface at the outlet of the vent pipe.

6. Summary and conclusions

The acoustic-structural FSI model was used for studying the chugging pressure source from the PPOOLEX experiments. Time signal of the source was taken from pressure measurement near the vent pipe exit, while the magnitude of the source and the pool response were scaled linearly to match with the experiment. The calculated pool pressures and wall motions corresponded qualitatively to the experiment, but there were significant quantitative differences. The pressure source magnitude varied roughly by a factor of 2 when different pressure sensor locations were used for the determination. However, much larger variations in the magnitude resulted depending on whether the drywell and vent pipe gas volumes were included in the model and on how the load was applied at the vent exit. Thus, the magnitude of the pressure source to be used in a simulation depends on the modelling details. The effect of FSI was found to be significant and the simulations with FSI agreed better with the experiment.

The scaling results obtained from earlier dimensional analyses (Sonin, 1981; Timperi et al., 2013) were studied by analytical and CFD calculations. The considered cases were the initial non-condensable phase of air discharge as well as oscillation of the water surface in the vent pipe and of the bubble. The earlier scaling result was found to agree approximately for the vent clearing when incompressible gas and velocity boundary were used in the modelling. After vent clearing, the linear time scaling $t \sim L$ resulted in too slow bubble rise and shedding in the small scale, as predicted by dimensional analysis of the bubble rise which yields $t \sim \sqrt{L}$. The analyses showed that for discharge through the open vent pipes, the hydrostatic pressure caused by the pipe submergence may be comparable to the drywell pressurization, i.e. negligible gravitation may not be justified in the dimensional analysis. This was the case at least in the PPOOLEX experiment SLR-05-02. In Timperi et al. (2013), the same scaling result was found for the steam bubble collapse as for the discharge transient if the pressure difference causing the collapse remains independent of system size. However, the hydrostatic pressure may affect the pressure difference, which would then depend on the system size and yield a different scaling result. In the calculations of the water surface oscillation frequency, the analytical and CFD results agreed well. The oscillation period scaled as $t \sim \sqrt{L}$ when only the gravitational effect was significant, while the period scaled as $t \sim L$ when only the pressure effect was significant.

Stochastic simulations of the BWR containment were continued by using the acoustic FSI model developed in the previous work (Timperi et al., 2013). Mesh sensitivity for the pool water, convergence of statistics and material damping were first studied. The mesh sensitivity study showed that the fairly coarse acoustic mesh of the pool water used in the simplified model is sufficient. Statistics of the pool structural response evaluated for different simulation durations indicated that the duration could be reduced to about 100 s. This resulted in about 50 chug events per pipe. The Rayleigh damping coefficients of the pool concrete structure were adjusted according to the most important eigenfrequencies of the pool. The new coefficients were fixed to yield 5 % of critical damping for 3 and 30 Hz. Characterization of the load shape of the chug events and simulations with different load shapes were then performed. The earlier load shape was scaled to full-scale from the PPOOLEX experiments, while the new load shapes were determined to better correspond the full-scale JAERI experiments presented by Kukita and Namatame (1985). The stochastic simulations were performed with two different water sonic velocities, i.e. 450 and 1412 m/s. The detailed load shape was found to have a relatively small effect on the pool structural response statistics. A more significant effect resulted from the water sonic velocity, namely the lower sonic velocity yielded clearly higher displacements in all cases. However, the sonic velocity was varied quite drastically. It would be of interest to vary also the duration of the chug event and time between each chug event, since these might have more influence on the pool structural response than the detailed load shape.

In modelling of the direct-contact condensation of large vapour bubbles, the basic features of the large scale interface model was implemented in ANSYS Fluent by using User-Defined Functions (UDFs). In the large scale interface mode, the surfaces of vapour bubbles larger than the grid size are tracked and resolved. The bubbles that are smaller than the grid size are modelled by using continuum approximation of the Euler-Euler two-phase model. In this sense, the model is a mixture of Volume Of Fluid (VOF) and Euler-Euler model.

The implemented large scale interface model was tested for the simulation of the MIX-03 experiment performed with the PPOOLEX facility. In this experiment, vapour is blown into the water pool of the wetwell and chugging occurs. The tracking of the large interfaces was demonstrated to perform properly. The condensation rate and the chugging frequency were, however, found to differ from the experimental observations. In the simulation, the condensation rate was too small and the chugging frequency was clearly too large. The numerical stability of the implemented model also remains to be improved.

Appendix A

The oscillation frequency of the gas-water interface in the condensation pool is analysed in the following with a simplified analytical model. The variables for static condition, i.e. no oscillation of the water surface, are defined as:

- p_1 drywell gas pressure
- p_2 wetwell gas pressure
- V_1 drywell gas volume
- V_2 wetwell gas volume
- A_1 area of water surface in the vent pipe
- A_2 area of water surface in the pool
- H_1 height of water column in the vent pipe
- H_2 height of water column in the pool above vent pipe outlet, i.e. $H_2 = H_1$ when the pressures in the drywell and wetwell are equal

For the oscillatory conditions, we define the deviations of the water surface from the static positions as:

- y_1 water surface deviation in the vent pipe
- y_2 water surface deviation in the pool

Here y_1 and y_2 are defined positive in the downwards and upwards directions, respectively. From the conservation of mass, assuming incompressible water, we have

$$y_1 A_1 = y_2 A_2 \tag{A.1}$$

For gas in the drywell and wetwell, we assume that the relation for adiabatic reversible compression holds (Wiksten, 1993):

$$\frac{T_0}{T} = \left(\frac{p_0}{p}\right)^{\frac{\gamma-1}{\gamma}} = \left(\frac{V}{V_0}\right)^{\gamma-1} \tag{A.2}$$

where γ is the ratio of specific heats. By considering that a volume V is subjected to a change ΔV, we have

$$1 + \frac{\Delta p}{p} = \left(1 + \frac{\Delta V}{V}\right)^{-\gamma} \tag{A.3}$$

By considering only small changes and remembering that

$$e^x = 1 + \frac{x}{1!} + \frac{x^2}{2!} + \frac{x^3}{3!} + \ldots \tag{A.4}$$

we obtain from Eq. (A.3)

$$\frac{\Delta p}{p} = -\gamma \frac{\Delta V}{V} \tag{A.5}$$

When the water surface in the vent pipe is deviated by a small amount y_1, we have changes in gas volume in the drywell and wetwell, respectively,

$$\Delta V_1 = y_1 A_1 = -\Delta V_2 = y_2 A_2 \tag{A.6}$$

From Eqs. (A.5) and (A.6), this results in a pressure difference change between drywell and wetwell as

$$\Delta p_p = -\Delta p_1 - \Delta p_2 = \gamma \frac{p_1}{V_1} y_1 A_1 + \gamma \frac{p_2}{V_2} y_2 A_2 \tag{A.7}$$

Using Eq. (A.1), this may be re-written

$$\Delta p_p = \gamma \left(\frac{p_1}{V_1} + \frac{p_2}{V_2} \right) y_1 A_1 \tag{A.8}$$

Similarly, the pressure difference change caused by gravitation is

$$\Delta p_g = \rho g (y_1 + y_2) \tag{A.9}$$

where ρ is the water density and g is the acceleration of gravity. Using Eq. (A.1), this may be re-written

$$\Delta p_g = \rho g y_1 (1 + A_1 / A_2) \tag{A.10}$$

Next, let us examine the dynamics of the water columns in the vent pipe and in the pool. Forces exerted on the water columns due to pressures at points 1, 2 and 3 (corresponding to water surface in the vent pipe, vent pipe outlet and water surface in the pool, respectively) are in the vent pipe and in the pool, respectively,

$$F_1 = (p_1 - p_3) A_1 \qquad F_2 = (p_3 - p_2) A_2 \tag{A.11}$$

Masses of the water columns in the vent pipe and in the pool are, respectively,

$$m_1 = \rho A_1 H_1 \qquad m_2 = \rho A_2 H_2 \tag{A.12}$$

From the Newton's second law we have

$$(p_1 - p_3) A_1 = m_1 \ddot{y}_1 \qquad (p_3 - p_2) A_2 = m_2 \ddot{y}_2 \tag{A.13}$$

where the dots denote differentiation with respect to time. Here we have made the simplified assumption that the water columns experience rigid-body motion and are connected through the pressure at point 3, i.e. at the vent pipe outlet. In reality, there is a region at the vent pipe outlet where the water velocity changes gradually from the value in the vent pipe to the (small) value in the pool. The size of this region is of order the diameter of the vent pipe for small amplitude oscillations.

Eliminating p_3 by combining Eqs. (A.13), inserting the masses of the water columns and noting that $\Delta p = p_2 - p_1$, we obtain after some re-arrangement

$$-\Delta p = \rho (H_1 \ddot{y}_1 + H_2 \ddot{y}_2) \tag{A.14}$$

Using Eq. (A.1), this becomes

$$-\Delta p = \rho \ddot{y}_1 (H_1 + H_2 A_1 / A_2) \tag{A.15}$$

Combining Eqs. (A.8), (A.10) and (A.15), we obtain an equation analogous to the linear second order differential equation for a mass-spring oscillator:

$$\underbrace{\rho\left(H_1 + H_2 \frac{A_1}{A_2}\right)}_{m} \ddot{y}_1 + \underbrace{\left[\gamma A_1\left(\frac{p_1}{V_1} + \frac{p_2}{V_2}\right) + \rho g\left(1 + \frac{A_1}{A_2}\right)\right]}_{k} y_1 = 0 \tag{A.16}$$

The natural frequency of this system is

$$f = \frac{1}{2\pi}\sqrt{\frac{k}{m}} = \frac{1}{2\pi}\sqrt{\frac{\gamma A_1 (p_1 / V_1 + p_2 / V_2) + \rho g (1 + A_1 / A_2)}{\rho (H_1 + H_2 A_1 / A_2)}} \tag{A.17}$$

References

Abaqus, 2012. Analysis User's Manual, Dassault Systèmes, Providence, RI, Version 6.12-1.

Björndahl, O. and Andersson, M., 1998. Globala vibrationer vid kondensationsförlopp i wetwell orsakade av LOCA i BWR-anläggningar. Swedish Nuclear Power Inspectorate, SKI Report 99:3, Stockholm, 81 p.

Coste, P., 2013. A Large interface model for two-phase CFD, Nuclear Engineering and Design, vol. 255, pp. 38–50.

Coste P, Pouvreau, J., Laviéville, J. and Boucker, M., 2008. A two-phase CFD Approach to the PTS Problem Evaluated on COSI Experiment, ICONE 16, Orlando, USA, May 11–15.

Kukita, Y. and Namatame, K., 1985. The vent-to-vent desynchronization effects on LOCA steam condensation loads in BWR pressure suppression pool. Nuclear Engineering and Design 85, pp. 141 - 150.

Laine, J., Puustinen, M. and Räsänen, A., 2009. PPOOLEX experiments with a modified blowdown pipe outlet. Lappeenranta University of Technology, Nuclear Safety Research Unit, Research report CONDEX 2/2008, 29 p. + app. 8 p.

Laviéville, J. and Coste, P., 2008. Numerical modelling of liquid-gas stratified flows using two-phase Eulerian approach, Proc. 5th Symposium on Finite Volumes for Complex Applications, Aussois, France, June 8-13.

Pättikangas, T., Niemi, J. and Timperi, A., 2011. Numerical modelling of pressure suppression pools with CFD and FEM codes. VTT Technical Research Centre of Finland, Research Report VTT-R-00927-11, Espoo, Finland, 53 p.

Puustinen, M., Laine, J. and Räsänen, A., 2011. Multiple blowdown pipe experiments with the PPOOLEX facility. Lappeenranta University of Technology, Nuclear Safety Research Unit, Research Report CONDEX 2/2010, 28 p. + app.8 p.

Sonin, A.A., 1981. Scaling laws for small-scale modelling of steam relief into water pools. Nuclear Engineering and Design, Vol. 65, pp. 17–21.

Timperi, A. 2009. Fluid-structure interaction calculations using a linear perturbation method. 20th International Conference on Structural Mechanics in Reactor Technology, Espoo, Finland, August 9 - 14, 2009.

Timperi, A., Chauhan, M., Pättikangas, T. and Niemi, J., 2012. Modeling of interaction of multiple vent pipes in a pressure suppression pool. VTT Technical Research Centre of Finland, Research Report VTT-R-01094-12, Espoo, Finland, 54 p.

Timperi, A., Chauhan, M., Pättikangas, T. and Niemi, J., 2013. Modelling of pressure loads in a pressure suppression pool. VTT Technical Research Centre of Finland, Research Report VTT-R-01563-13, Espoo, Finland, 55 p.

Wiksten, R., 1993. Lämpövoimaprosessit. Teknillinen korkeakoulu, Energiatekniikan laitos, Otaniemi.

Wiksten, R., 1995. Virtauskoneet. Teknillinen korkeakoulu, Energiatekniikan laitos, Otaniemi.

Bibliographic Data Sheet **NKS-308**

Title	CFD and FEM simulations of pressure suppression pool behaviour
Author(s)	Antti Timperi, Timo Pättikangas and Jarto Niemi
Affiliation(s)	VTT Technical Research Centre of Finland
ISBN	978-87-7893-386-7
Date	June 2014
Project	NKS-R / ENPOOL
No. of pages	53
No. of tables	5
No. of illustrations	40
No. of references	15

Abstract
max. 2000 characters

"The large interface model" published recently by P. Coste has been studied. The interface tracking model of Coste has been implemented in Fluent. The direct-contact condensation model has been modified so that the grid cells adjacent to the interface cell are also used in the heat transfer calculation. Simulations of short period of the chugging phase of the PPOOLEX experiment MIX-03 have been performed.

Modelling of the PPOOLEX experiment COL-01 has been performed with the acoustic-structural FEM model. Different values for the pool structural damping were first tested to find a damping value giving best agreement with the experiment. Simulations with three different values of water sonic speed have been performed and compared with the experiment. The effects of including the drywell gas to the acoustic model and applying the pressure source at the vent pipe outlet have been studied.

Studies of scaling of the measurements to full scale geometry have been performed. Simulations of the beginning of the blowdown have been performed with the new Star-CCM+ code and compared with the scaling results from 2012. Oscillation frequency of the water surface in the vent pipe has also been studied with an analytical model. The oscillation frequency has been calculated with Star-CCM+ and compared with the analytical results.

The coefficients for the Rayleigh damping of the structure have been studied. A mesh sensitivity study has been performed. Characterization of the pressure pulse has been started; simulations with different shapes of pressure pulses have been performed to study the effect of the shape. Convergence of the containment response statistics has been examined by evaluating the statistics for signals of different length.

Key words: Condensation pool, pressure suppression pool, BWR, CFD, fluid-structure interaction, FSI, chugging, LOCA

Available on request from the NKS Secretariat, P.O.Box 49, DK-4000 Roskilde, Denmark.
Phone (+45) 4677 4041, e-mail nks@nks.org, www.nks.org